

# **COMPUTATIONAL INVESTIGATION OF PERFLUOROCARBON-GAS BUBBLE DYNAMICS IN THREE-DIMENSIONAL BIFURCATING ARTERIES.**



A thesis report submitted in partial fulfillment of the requirement for the degree  
of  
Bachelor of Science in Mechanical Engineering

Submitted By  
Chinmoy Deb Nath  
Student ID: 1903082

Supervised by:

Dr. Md. Mamunur Roshid  
Professor.

**Department of Mechanical Engineering**

---

**Chittagong University of Engineering & Technology  
Chattogram-4349, Bangladesh**

**CHITTAGONG UNIVERSITY OF ENGINEERING AND TECHNOLOGY,  
CHATTOGRAM**

**(PROJECT AND THESIS)**

**COURSE NO.: ME 498**

**Title of the Project: Computational Investigation of Perfluorocarbon-Gas Bubble Dynamics in Three-Dimensional Bifurcating Arteries.**

**Name of the Student: Chinmoy Deb Nath**

**Student ID: 1903082**

**Session: 2022-2023**

**Name of the Department: Mechanical Engineering**

**Program: B. Sc. Eng.**

**Name of the Supervisor: Dr. Md. Mamunur Roshid**

**Professor**

**Department of Mechanical Engineering, CUET**

**Signature of the Student**

**Signature of the Supervisor**

# Abstract

A better understanding of bubble dynamics in blood vessels can improve medical treatment and physiological processes. Considering the non-Newtonian features of blood and perfluorocarbon gas, this study uses numerical simulation to investigate the dynamics of bubbles and their division inside a vascular network.

This numerical study investigates the splitting dynamics of perfluorocarbon (PFC) gas bubbles in symmetric vascular bifurcations ( $60^\circ$ ,  $90^\circ$ ,  $120^\circ$ ) under physiological flow conditions ( $Re = 100$ ). Using the volume of fluid method in ANSYS Fluent with a Carreau non-Newtonian blood model, bubble transport, deformation, and splitting behavior are analyzed. The simulations reveal homogeneous bubble splitting across all bifurcation angles, with  $90^\circ$  bifurcations exhibiting the most efficient division. Key findings include: (1)  $60^\circ$  bifurcations demonstrate stable flow with convex bubble neck formation, (2)  $120^\circ$  cases show flow instability and concave neck shapes leading to satellite bubble formation, and (3) non-Newtonian effects reduce splitting time variability compared to Newtonian predictions. The results provide critical insights for optimizing gas embolotherapy protocols and vascular device designs, particularly regarding angle-dependent bubble behavior and flow stability.

This study enhances the understanding of bubble dynamics in non-Newtonian blood flow by clarifying how bubble splitting affects bubbles of various sizes. The findings can help improve the efficiency of oxygen delivery in certain areas and optimize vessel designs. Research into bubble-related phenomena and their health implications can also benefit greatly from this numerical simulation method.

# Acknowledgment

With sincere gratitude to the Almighty, I would like to take the privilege to express my appreciation to Dr. Md. Mamunur Roshid, Professor in the Department of Mechanical Engineering at CUET, for his unwavering support, direction, and encouragement throughout my research journey. His vast knowledge and insightful perspectives have profoundly influenced my work.

I sincerely thank the esteemed faculty members of the Department of Mechanical Engineering at CUET for their valuable contributions and constructive criticism. I must thank my peers for their constant support and companionship, which made this journey truly enjoyable.

For their unwavering support, love, and steadfast belief in me, I will be eternally indebted to my family. Their constant encouragement has been a constant source of motivation.

Lastly, I want to express my profound thankfulness to everyone who inspired me to complete this journey.

July 2025

CUET

Author

Chinmoy Deb Nath

ID: 1903082

## **Table of Contents**

Abstract.....	i
Acknowledgment.....	ii
CHAPTER 1 .....	1
1.1    Fluid Mechanics.....	1
1.1.1    Fluid statics .....	1
1.1.2    Fluid dynamics .....	1
1.2    Bubble Dynamics.....	6
1.2.1    bubble formation in gas-liquid system.....	6
1.3    Hemodynamics .....	12
1.3.1    Blood .....	12
1.3.2    Blood flow.....	13
1.3.3    Blood Velocity .....	14
1.3.4    Turbulence.....	14
1.3.5    Wall tension.....	15
1.3.6    Blood pressure.....	15
1.4    Research Objectives.....	17
CHAPTER 2 .....	18
2.1    Introduction:.....	18
2.2    Bubble Dynamics in Therapeutic Applications .....	18
2.3    The Behavior of Bubbles in Hemodynamic Flow .....	20
2.4    Stability of Bubble .....	23
2.5    Bubble-capillary wall interaction.....	24
2.6    Research Gap: .....	26
CHAPTER 3 .....	27
3.1    Numerical Simulation .....	27
3.1.1    Dimensions of the model.....	27

3.2	Numerical Modelling .....	28
3.3	Governing Equations .....	29
3.4	Procedure flow diagram .....	31
3.5	Thesis structure diagram .....	32
CHAPTER 4 .....		33
4.1	Introduction.....	33
4.2	Meshing .....	33
4.2.1	Grid generation.....	33
4.2.2	Mesh independence test: .....	34
4.2.3	Mesh quality.....	35
4.3	Simulation setup .....	36
4.3.1	Initialization .....	36
4.3.2	Model configuration.....	36
4.3.3	Multiphase Model .....	37
4.3.4	Boundary Conditions.....	37
4.3.5	Solution methods.....	38
CHAPTER 5 .....		41
5.1	Introduction.....	41
5.2	Vessels with bifurcation angles .....	41
5.2.1	60° bifurcation angle .....	41
5.2.2	90° bifurcation angle .....	49
5.2.3	120° bifurcation angle .....	56
5.3	Model Validation Against Published Numerical Study .....	62
CHAPTER 6 .....		64
6.1	Conclusions.....	64
6.2	Future work .....	65
References .....		66

## List of Figures

Figure 1-1 :Newtonian and Non-Newtonian Fluids [10] .....	4
Figure 1-2 :Steady and Unsteady Flow [11]. .....	5
Figure 1-3 :The transition from laminar to turbulent flow [10]. .....	6
Figure 3-1: Schematic diagram of the bifurcation geometry.....	28
Figure 3-2: 3D model Geometries.....	28
Figure 3-3 :Procedure flow diagram.....	31
Figure 3-4: Thesis structure diagram.....	32
Figure 4-1: $60^\circ$ , $90^\circ$ , $120^\circ$ bifurcation angles respectively.....	34
Figure 4-2: Transient Setup .....	36
Figure 4-3: Materials Setup .....	37
Figure 4-4: Multiphase Model Setup.....	37
Figure 4-5: Fully developed parabolic velocity profile (Top-Left) & Boundary Conditions... .....	38
Figure 4-6: Initial Bubble Position. ....	39
Figure 4-7: Solution Methods (left), Run Calculation (right). ....	40
Figure 5-1:PFC bubble behavior at different time instances for $60^\circ$ Bifurcation Vessel. ....	42
Figure 5-2: Velocity Contours at different time instances of $60^\circ$ Bifurcation Vessel.....	44
Figure 5-3: Pressure Contours at different time instances of $90^\circ$ Bifurcation Vessel. ....	47
Figure 5-4: Velocity-u and Velocity-v Profiles of $60^\circ$ Bifurcation Vessel.....	49
Figure 5-5: PFC bubble behavior at different time instances for $90^\circ$ Bifurcation Vessel. ....	50
Figure 5-6: Velocity Contours at different time instances of $90^\circ$ Bifurcation Vessel.....	52
Figure 5-7: Pressure Contours at different time instances of $90^\circ$ Bifurcation Vessel. ....	54
Figure 5-8: Velocity-u and Velocity-v Profiles of $60^\circ$ Bifurcation Vessel.....	55
Figure 5-9: PFC bubble behavior at different time instances for $90^\circ$ Bifurcation Vessel. ....	56
Figure 5-10: Velocity Contours of $120^\circ$ Bifurcation Vessel at different time instances.....	58

Figure 5-11: Pressure Contours at different time instances of 120° Bifurcation Vessel.....	60
Figure 5-12: Velocity-u and Velocity-v Profiles of 60° Bifurcation Vessel.....	61
Figure 5-13: Splitting Behavior of vessels with varying angles.....	62
Figure 5-14 Splitting behavior of PFC bubble at the bifurcation point.....	62
Figure 5-15: Small satellites retaining in vessel of 120° bifurcation angle.....	63

## **List of Tables**

Table 1-1: Relations of the flow velocity of blood with X-section area of vessels[22]. .....	14
Table 4-1: Mesh Independence study .....	35
Table 4-2: Mesh Quality. ....	36
Table 6-1: Comparative study of findings. ....	65

# CHAPTER 1

## INTRODUCTION

### 1.1 FLUID MECHANICS

Fluid mechanics is a branch of physics that studies how fluids (liquids, gases, and plasmas) behave and the forces that act on them [1]. It can be used in many fields such as engineering (chemical, mechanical, aerospace, biomedical, and civil ), as well as in areas like earth science, ocean studies, weather forecasting, space science, and biology.

The field can be divided into two main parts: fluid statics, which studies fluids when they are at rest, and fluid dynamics, which looks at how forces affect the movement of fluids [2]. Fluid dynamics is a challenging and mathematically difficult area of study. Many problems are still not fully solved and are best addressed using numerical techniques, often with the help of computers. A field known as computational fluid dynamics (CFD) focuses on this method [3].

#### 1.1.1 Fluid statics

Fluid statics, or hydrostatics, is a branch of fluid mechanics that focuses on fluids at rest. It studies how fluids stay balanced and in a stable state, unlike fluid dynamics, which deals with fluids that are moving.

Hydrostatics helps explain everyday phenomena, like how air pressure changes with altitude, why objects like wood and oil float on water, and why the water level stays the same in containers, no matter their shape.

This area of study is essential for hydraulics, the branch of engineering that deals with fluid management. Hydrostatics also plays an important role in fields like geophysics (for understanding things like plate movements and Earth's gravity), weather science, and even medicine, especially when looking at blood pressure [2].

#### 1.1.2 Fluid dynamics

Fluid dynamics is a part of fluid mechanics that studies how fluids, both liquids and gases, move and the rules that control their movement [4]. Fluid dynamics forms the basis for many

practical fields. It combines observed and calculated principles from flow measurements to solve real-world problems. When tackling a fluid dynamics issue, the focus is on key fluid characteristics such as speed, pressure, density, and temperature, which can change over time and space. This wide-reaching field includes subareas like aerodynamics (studying gases like air in motion) and hydrodynamics (studying liquids in motion). Fluid dynamics is used in many ways, from calculating forces on aircraft to measuring the flow of oil in pipelines. It's essential for weather forecasting, studying space objects like nebulae, and understanding explosions. It also applies to various fields such as traffic management and studying how populations change over time [1].

#### *1.1.2.1 Conservation laws*

Fluid dynamics problems are approached using three main conservation laws, which can be written in either integral or differential forms. These laws are applied to a specific area called a control volume, which is the region where fluid is assumed to flow. The integral form of these laws looks at changes in mass, momentum, or energy within the control volume. In contrast, the differential form uses Stokes' theorem to create a formula that describes the integral form of the law at an extremely small volume at a particular point in the flow.

##### 1.1.2.1.1 Conservation of mass

The change in mass of fluid within a controlled volume must match the net fluid flow rate entering the volume. This ensures that mass is conserved within the control volume [5], and can be expressed as the continuity equation's integral form :

$$\frac{\partial}{\partial t} \iiint_v \rho \, dv = - \oint \rho \vec{u} \cdot d\vec{s} \quad (1)$$

The symbols have the same meaning as they are commonly used for in the equation.

##### 1.1.2.1.2 Conservation of momentum

Newton's 2nd law of motion in control volume, states that any alteration in the fluid's momentum inside that volume is due to the net momentum influx and the influence of external forces acting on the fluid inside the container.

$$\frac{\partial}{\partial t} \iiint_V \rho \mathbf{u} dV = - \iiint_S (\rho \mathbf{u} \cdot \mathbf{dS}) \mathbf{u} - \iiint_S \mathbf{p} dS + \iiint_V \rho \mathbf{f}_{bd} dV + \mathbf{F}_{surf} \quad (2)$$

In this equation, the left side represents the total change in momentum within the volume. The first term on the right side shows the rate at which momentum is moving into the volume. The second term on the right represents the force exerted by pressure on the volume's surfaces. These two terms are subtracted because momentum entering the system is considered positive, and the direction opposite to the velocity and pressure forces is taken into account. The third term on the right indicates the net acceleration of the mass within the volume due to body forces (denoted by  $\mathbf{f}_{bd}$ ). Surface forces, including viscous forces, are represented by  $\mathbf{F}_{surf}$  which shows the total force from shear forces acting on the volume's surface. Momentum balance can also be expressed for a dynamically controlled volume [6].

#### 1.1.2.1.3 Conservation of energy

In a closed system, the total energy stays the same, although it can change from one type to another.

$$(\rho \frac{Dh}{Dt} = \frac{Dp}{Dt} + \nabla \cdot (\mathbf{k} \nabla T) + \Phi) \quad (3)$$

In this context,  $h$  stands for specific enthalpy,  $k$  represents the fluid's heat conductivity, and  $T$  denotes temperature.  $\Phi$  is the viscous dissipation function, which controls how quickly mechanical energy in the flow is turned into heat energy. According to the second law of thermodynamics, this dissipation term must always be positive, meaning that viscosity cannot create energy within the control volume [7].

#### 1.1.2.2 *Compressible and Incompressible Flow*

Compressible flow, also known as gas dynamics, is a field of fluid mechanics that focuses on flows where the fluid's density changes. Although all flows can technically be considered compressible, they are often treated as incompressible when the Mach number is under 0.3 because density variations in this range are small, around 5%. The study of compressible flow is crucial for high-speed aircraft, jet engines, rocket propulsion, rapid atmospheric entry, gas pipelines, industrial processes like abrasive blasting, and numerous other applications [8].

In fluid mechanics, incompressible flow (or isochoric flow) refers to a flow where the density of fluid remains constant over time. This means that the flow velocity's divergence is zero.

However, this does not imply that the fluid is truly incompressible. In some cases, the flow of compressible fluids can be treated as incompressible for simplicity, especially when changes in density are minimal [9].

#### *1.1.2.3 Newtonian and non-Newtonian fluids*

The key difference between Newtonian and non-Newtonian fluids is how their viscosity behaves. Viscosity is the resistance of a fluid to flow or change shape, and all fluids, except superfluids, have some degree of viscosity. Newtonian fluids, like water and air, show a simple, direct relationship between the stress from viscous forces and the rate at which the fluid changes shape (strain rate). In these fluids, viscosity stays constant no matter how much the fluid is deformed. In contrast, non-Newtonian fluids have a more complex, non-linear relationship between stress and strain rate. These fluids, which include emulsions, slurries, blood, certain polymers, and thick substances like latex, honey, and lubricants, are studied in a field called rheology [2].

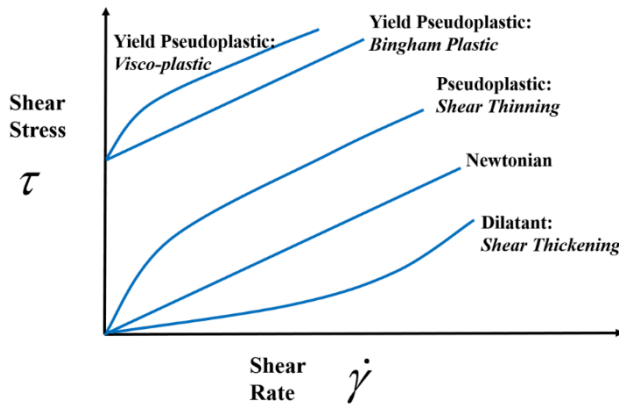


Figure 1-1 :Newtonian and Non-Newtonian Fluids [10]

#### *1.1.2.4 Steady and unsteady flow*

A steady flow occurs when the fluid properties at a specific point do not change over time. In contrast, unsteady or transient flow varies with time. The stability of the flow can depend on the reference frame used to observe it [1].

Even though turbulent flows are not steady, they can exhibit statistical stationarity, meaning their statistical properties remain constant over time. The equations for a steady problem have

one fewer dimension (time) compared to those for a problem with a constant flow field. Because of this, the analysis of steady flows is simpler than that of turbulent flows [2].

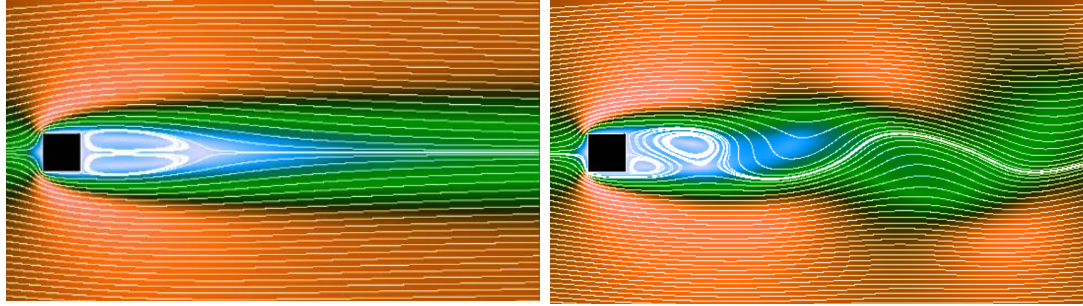


Figure 1-2 :Steady and Unsteady Flow [11].

#### 1.1.2.5 *Laminar and turbulent flow*

Turbulent flow is marked by recirculation, eddies, and unpredictability. Laminar flow, on the other hand, is characterized by the absence of turbulence. It is prone to the formation of eddies and recirculation. Reynolds decomposition is employed for the mathematical modeling of turbulent flow. This decomposition divides the flow into average and disturbance components. The Navier-Stokes equations can accurately depict turbulent flows. Direct numerical simulation (DNS) can replicate turbulent flows with moderate Reynolds numbers utilizing the Navier-Stokes equations. Nonetheless, considering the present capabilities of processing power, DNS is not a viable option for the majority of pertinent flows due to their excessively huge Reynolds numbers. Therefore, turbulence models are vital for tackling practical flow problems. Scientists rely on models based on the Reynolds-averaged Navier-Stokes equations (RANS) and incorporate turbulence models to predict the behavior of turbulent flow. Detached eddy simulation (DES), which integrates the RANS turbulence model with large eddy simulation, is a compelling technology.



Figure 1-3 :The transition from laminar to turbulent flow [10].

## 1.2 BUBBLE DYNAMICS

A bubble is a spherical entity of gas that forms within a liquid. Conversely, a droplet of liquid suspended in a gas is referred to as a drop [10]. Bubble dynamics is the study of how bubbles oscillate, grow, form, and collapse in fluids, depending on various physical and environmental factors. Gas-filled cavities can be produced via mechanical agitation, thermal processes, or sonic stimulation. Bubbles display a diverse array of captivating and complicated behaviors, including the production of light (sonoluminescence), sound, and shock waves, along with elaborate motion patterns such as spirals or zigzags [11]. The examination of bubbles is both scientifically fascinating and practically significant. Bubble dynamics applications encompass several domains, including the reduction of hydrodynamic drag, the facilitation of targeted medication delivery, the fragmentation of kidney stones by lithotripsy, and the promotion of effective surface cleaning [12].

### 1.2.1 BUBBLE FORMATION IN GAS-LIQUID SYSTEM

The generation of bubbles is affected by the interaction of liquid pressure, surface tension, and bubble size in gas-liquid systems. Cavitation in liquids, analogous to cracking in solids, transpires when negative pressure induces voids. The equation defining the equilibrium of a bubble can be articulated as:

$$pv - pl = \frac{2\pi\gamma}{R_b} \quad (4)$$

where  $p\nu$  resembles the vapor pressure inside the bubble,  $pl$  is the liquid pressure,  $\gamma$  is the surface tension, and  $R_b$  is the radius of bubble. When  $pl$  drops below  $p\nu - \frac{2\pi\gamma}{R_b}$ , the bubble expands, causing liquid rupture. Surface tension, indicative of intermolecular forces, is pivotal in the stabilization or destabilization of bubbles, particularly under fluctuating pressures and bubble diameters. This dynamic is essential for comprehending the mechanisms of bubble generation and its applications in industrial and chemical operations [13].

#### 1.2.1.1 The energy cost of forming a bubble

The formation of bubbles in a liquid requires the input of free energy, which can be described using several constants and the radius of the bubble. According to scaled particle theory, the free energy associated with cavity formation may be articulated about the properties of the solvent and solute, as well as pressure and temperature. The free energy of cavity formation,  $\Delta G_{\text{cav}}$ , can be expressed by the subsequent equation:

$$(\Delta G_{\text{cav}} = K_0 + K_1 R_b + K_2 R_b^2 + K_3 R_b^3) \quad (5)$$

where  $R_b$  is the bubble radius, and constants  $K_0$ ,  $K_1$ ,  $K_2$ ,  $K_3$  depend on the properties of the solvent and solute. The constants can be further defined as:

$$K_0 = R T \left[ -\ln(1-y) + \left( \frac{y}{1-y} \right)^2 \right] - \frac{\pi p a^3}{6} \quad (6)$$

$$K_1 = -\frac{RT}{a} \left[ \frac{6y}{1-y} + 18 \left( \frac{y}{1-y} \right)^2 \right] + \pi p a^2 \quad (7)$$

$$K_2 = \frac{RT}{a^2} \left[ \frac{12y}{1-y} + 18 \left( \frac{y}{1-y} \right)^2 \right] - 2\pi p a \quad (8)$$

$$K_3 = \pi p \quad (9)$$

$a$  is the diameter of the solvent hard-sphere,  $\frac{\pi p a^3}{6}$  is the volumetric portion of the solvent spheres,  $\rho$  is the pure solvent's total density,  $p$  is the pressure,  $R$  as the gas constant.

### 1.2.1.2 Governing Equations of Bubble Dynamics

Bubble dynamics are regulated by a series of equations that delineate the behavior of bubbles within a fluid under diverse conditions. These equations take into account the impact of pressure, surface tension, viscosity, and inertial forces on the creation, growth, oscillation, and collapse of bubbles.

#### 1.2.1.2.1 Rayleigh–Plesset's equation

The Rayleigh–Plesset's equation is a principal nonlinear ordinary differential equation that characterizes the behavior of a bubble in an incompressible, viscous fluid. It represents the equilibrium of inertial, pressure, viscous, and surface tension forces exerted on the bubble. The equation is articulated as :

$$R\ddot{R} + \frac{3}{2}\dot{R}^2 = \frac{1}{\rho} \left( P_g - P_0 - P(t) - \frac{4\mu\dot{R}}{R} - \frac{2\sigma}{R} \right) \quad (10)$$

The equation incorporates the bubble radius ( $R$ ) and its time derivatives ( $\dot{R}$  and  $\ddot{R}$ ), alongside fluid variables such as density ( $\rho$ ) and viscosity ( $\mu$ ). The gas pressure of the bubble ( $P_g$ ), the liquid pressure  $P_0$ , and the acoustic wave pressure  $P(t)$  has been discussed. This equation is essential for comprehending phenomena like cavitation and sonoluminescence, where bubble dynamics are critical [14], [15].

#### 1.2.1.2.2 Keller–Miksis Equation

The Keller–Miksis equation enhances the Rayleigh–Plesset framework by integrating liquid compressibility effects, rendering it more appropriate for modeling high-amplitude bubble oscillations where acoustic waves play a crucial role. The equation is expressed as:

$$\left(1 - \frac{\dot{R}}{c}\right) R\ddot{R} + \frac{3}{2} \left(1 - \frac{\dot{R}}{3c}\right) \dot{R}^2 = \frac{1+\frac{\dot{R}}{c}}{\rho} \left( P_b(t) - P_\infty(t) - \frac{2\sigma}{R} - \frac{4\mu\dot{R}}{R} \right) \quad (11)$$

This equation offers a more precise depiction of bubble dynamics in compressible fluids, particularly under swift dynamic conditions. Developed by Joseph B. Keller and Michael Miksis in 1980, it aimed to overcome the limits of the Rayleigh–Plesset equation in specific settings [16], [17].

#### 1.2.1.2.3 Gilmore Equation

The Gilmore equation enhances the modeling of bubble dynamics by comprehensively incorporating liquid compressibility and shock wave propagation. It is especially beneficial for examining violent bubble contractions and expansions. The equation is expressed as :

$$\left(1 - \frac{\dot{R}}{c}\right) R \ddot{R} + \frac{3}{2} \left(1 - \frac{\dot{R}}{3c}\right) \dot{R}^2 = \left(1 + \frac{\dot{R}}{c}\right) \left( \frac{P_b(t) - P_\infty(t)}{\rho} + \frac{R}{c} \frac{d}{dt} \frac{P_b(t) - P_\infty(t)}{\rho} \right) \quad (12)$$

This equation is crucial for situations involving significant pressure differentials and swift bubble dynamics, as observed in medical ultrasonography applications and underwater detonations. Forrest Gilmore presented this concept in 1952 to tackle the complications associated with liquid compressibility [16].

#### 1.2.1.2.4 Volume of Fluid (VOF) Numerical Approach

The VOF approach is a numerical tool to monitor and identify free surfaces or fluid-fluid interfaces in CFD simulations. It is especially adept at modeling intricate interfacial events, including bubble formation, coalescence, and breakup. The VOF approach entails resolving a continuous equation for the volume fraction of one fluid,

$$\frac{\partial F}{\partial t} + u \cdot \nabla F = 0 \quad (13)$$

where  $F$  represents the volume fraction of the fluid within a computational cell and  $u$  is the velocity vector.

#### *1.2.1.3 Applications of Bubble Dynamics*

The examination of bubble dynamics, especially regarding viscoelastic fluid interfaces, possesses significant significance in numerous industrial and medicinal domains. Presented below are several principal applications resulting from the research:

**Localized Chemotherapy Delivery:** Microbubbles facilitate the targeted delivery of chemotherapy medicines to cancer cells, thereby minimizing systemic toxicity and enhancing the effectiveness of treatments such as doxorubicin, which is constrained by adverse effects including cardiotoxicity and nephrotoxicity [18].

**Cardiovascular Disease Treatment:** They can transport pharmaceuticals and genetic substances to targeted regions impacted by cardiovascular ailments, including atherosclerotic plaques and thrombi [18].

**Brain Drug Delivery:** Microbubbles are being investigated for their potential in medicine delivery to the brain, addressing the obstacle posed by the blood-brain barrier [18].

**Ultrasound Contrast Agents:** Initially developed to enhance ultrasound imaging, microbubbles improve the acoustic signal from blood, aiding in better diagnosis and monitoring [18].

**Stability and Encapsulation:** Enhancements in microbubble stability via encapsulation with substances such as lipids, proteins, and polymers have rendered them more efficient for imaging and medication administration [18].

**Targeted Drug Delivery:** Microbubbles can be modified with ligands for targeted adherence, guaranteeing accurate medication delivery to the intended site [18].

**Food Industry:** Comprehending bubble dynamics helps improve processes such as aeration and emulsification, essential for creating food products with preferred textures and flavors. The efficacy of bubble ascent and their interactions with liquid interfaces might affect the quality of food production processes [19].

**Pharmaceuticals:** The dynamics of bubbles in complicated fluids can influence the delivery and stability of active pharmaceutical components in medication formulation. Optimizing bubble dynamics enables manufacturers to enhance the efficacy and shelf-life of pharmaceutical items [19].

**Chemical Engineering:** The principles of bubble dynamics are essential in processes like mixing, reaction kinetics, and mass transfer. The research emphasizes the capacity of surfactants and nanoparticles to alter bubble dynamics, which can be utilized to improve chemical reactions and separations [19].

**Sewage Purification:** Research demonstrates that bubble dynamics influence sewage treatment procedures. Comprehending the dynamics of bubble ascent and their interaction with pollutants can enhance the efficacy of purification systems, resulting in improved environmental results [19].

**Material Science:** The research on the role of nanoparticles and surfactants on bubble dynamics can guide the creation of novel materials with targeted characteristics. Controlling

bubble behavior can result in advancements in foams and emulsions utilized in diverse applications, ranging from packaging to construction materials [19].

**Environmental Engineering:** The examination of bubble dynamics can also aid with environmental technologies, such as air sparging and bioremediation, where bubbles facilitate the decomposition of pollutants in water and soil [19].

**Underwater explosion bubbles:** Underwater explosive bubbles are essential in naval construction and marine engineering. These bubbles arise following a shockwave from an explosion, resulting in high pressure and temperature formations. Upon the collapse of a bubble, it produces high-velocity liquid jets (about 100 m/s) capable of inflicting significant structural damage, including compromising a ship's longitudinal integrity. Such studies are essential for evaluating the effects of underwater explosions on maritime structures and enhancing ship resistance [20].

**High-pressure air gun bubbles:** Air cannon bubbles are crucial for deep-sea resource extraction and scientific inquiry. Air cannons produce high-pressure bubbles that generate seismic waves for mapping the seafloor and identifying resources such as oil, gas, and flammable ice. Engineers refine air gun arrays to improve signal quality and reduce bubble pulsations, facilitating accurate and efficient resource exploration [20].

**Spark and laser bubbles:** Spark and laser bubbles are extensively utilized in environmental engineering, mechanical systems, and medicine. They are easier to produce and examine than exploding bubbles, frequently acting as a replacement in experimental investigations of bubble dynamics. Applications encompass ice cracking, surface cleaning, and the investigation of pulsation mechanisms at boundaries [20].

**Water entry/exit cavitation bubbles:** These are bubbles that are caused by the high-speed motion of a structure entering or exiting water, such as a missile, a torpedo, or a wave slamming on a ship. The study of water entry/exit cavitation bubbles can help predict the hydrodynamic loads, structural responses, and damage effects of the water impact problems [20].

**Propeller cavitation bubbles:** These are bubbles generated by the rapid movement of a structure entering or departing water, such as a missile, a torpedo, or a wave impacting a vessel. The examination of water entrance and exit cavitation bubbles can facilitate the prediction of hydrodynamic stresses, structural reactions, and damage effects associated with water impact issues [20].

**Rising Bubbles:** Rising bubbles are examined in multiphase fluid mechanics, with applications in oceanic and chemical engineering. These bubbles affect phenomena such as buoyancy-driven flows and gas-liquid interactions. Their course, frequently zigzag or spiral, is influenced by wake effects, surface tension, and viscosity, which are crucial in industrial reactors and environmental research [20].

### 1.3 HEMODYNAMICS

Hemodynamics is the study of blood flow and the forces that influence it within the circulatory system. The circulatory system operates under homeostatic mechanisms, similar to control systems in hydraulic circuits. Hemodynamics continuously monitors and adjusts to both physiological and environmental conditions. It explains the physical principles that control blood flow throughout the vascular system.

Blood circulation allows for the transport of oxygen, hormones, nutrients, metabolic wastes, and carbon dioxide throughout the body. This process supports cellular metabolism, regulates pH, osmotic pressure, and body temperature, and helps protect against infections and physical injuries [21].

Blood is a non-Newtonian fluid, which means its flow is better understood through rheology instead of traditional hydrodynamics. Since blood vessels are flexible, the techniques used in classical fluid mechanics, such as those relying on viscometers, don't fully capture the complexities of hemodynamics. The study of blood circulation is known as hemodynamics, while the study of the properties of blood flow itself is called hemorheology [22].

#### 1.3.1 BLOOD

Blood is a complex fluid consisting of plasma and cellular components. Plasma is made up of 91.5% water, 7% proteins, and 1.5% various solutes. The cellular elements include platelets, leukocytes, and erythrocytes. The way these cells interact with the plasma molecules is the primary reason why blood doesn't behave like an ideal Newtonian fluid [21].

### 1.3.2 BLOOD FLOW

The heart acts as the pump of the circulatory system, pushing blood through the body with each beat. The amount of blood the heart pumps out, usually measured in liters per minute, is called cardiac output (CO). Blood leaves the heart and travels into the aorta, the body's largest artery. From there, it branches out into smaller arteries, arterioles, and eventually reaches the capillaries, where oxygen is exchanged. These tiny capillaries connect to venules, which then guide the blood back through the veins to the venae cavae and into the right atrium of the heart.

The network of arterioles, capillaries, and venules, known as microcirculation, takes up most of the circulatory system's area and is where oxygen, glucose, and other nutrients are delivered to cells. The veins carry the deoxygenated blood back to the right atrium, where it's then pumped to the lungs to collect fresh oxygen and release carbon dioxide and other waste gases. After that, the blood returns to the left side of the heart, and the cycle starts over again. In a typical circulatory system, the amount of blood returning to the heart each minute is roughly the same as the volume the heart pumps out each minute (the cardiac output) [23]. The velocity of blood flow at various points in the circulatory system is primarily influenced by the total cross-sectional area at each level. Cardiac output can be measured using different methods, one of which is the Fick equation:

$$CO = \frac{VO_2}{CaO_2 - CvO_2} \quad (14)$$

CO represents cardiac output, conventionally quantified in liters per minute (L/min). VO<sub>2</sub> denotes oxygen consumption, typically quantified in milliliters per minute (mL/min). CaO<sub>2</sub> denotes the arterial oxygen content, quantified in milliliters of oxygen per liter of blood (mL O<sub>2</sub>/L). CvO<sub>2</sub> denotes the venous oxygen content, quantified in milliliters of oxygen per liter of blood (mL O<sub>2</sub>/L). The thermodilution method involves injecting a fluid with a known temperature into the Swan-Ganz catheter's proximal port and then measuring how much the temperature changes at the distal port. By analyzing this temperature shift, cardiac output can be calculated using a specific formula. This process helps estimate how much blood the heart pumps out each minute.

$$CO = SV \times HR \quad (15)$$

Cardiac output (CO) is the amount of blood the heart pumps per minute, measured in liters. It's calculated by multiplying stroke volume (SV) by heart rate (HR). At rest, normal CO is about 5 to 6 liters per minute. The blood left in the ventricle after contraction is the end-systolic volume (ESV), found by subtracting stroke volume from end-diastolic volume (EDV)[23].

### 1.3.3 BLOOD VELOCITY

Blood velocity is usually measured in centimeters per second (cm/s). It decreases as the cross-sectional area of the vessel increases and varies with the size of the blood vessels. Since blood flow is typically laminar, the velocity is fastest at the center of the vessel and slowest near the walls. For most calculations, the average velocity is used[24]. Blood flow velocity can be quantified by several methods, such as microscopy of capillaries with frame analysis or laser-Doppler velocimetry [25]. Blood velocity in arteries is higher during systole compared to diastole. The pulsatility index (PI) quantifies this difference by calculating the difference between maximum and minimum diastolic velocity which is then divided by the average velocity. This value decreases as the distance from the heart increases [26].

Table 1-1: Relations of the flow velocity of blood with X-section area of vessels[22].

Blood vessel Type	X-section area (cm <sup>2</sup> )	Blood velocity (cm/s)
Aorta	3 – 5	40
Capillaries	4500 – 6000	0.03 [27]
Vena cavae	14	15

### 1.3.4 TURBULENCE

The smoothness of the veins influences the flow of blood which then leads to either chaotic or smooth flow. The buildup of fatty deposits on artery walls reduces their smoothness. The Reynolds number aids in assessing the behavior of a fluid within a conduit, namely blood within a vessel. The formula for this dimensionless correlation is expressed as: [28]

$$Re = \frac{\rho v L}{\mu} \quad (16)$$

Here,  $\rho$  represents the density of the blood,  $v$  is the average velocity,  $L$  is the diameter of the vessel, and  $\mu$  is the viscosity of the blood. The Reynolds number ( $Re$ ) depends on both the velocity and the vessel's diameter. When the Reynolds number is below 2300, the flow is laminar, meaning it's smooth and steady. If it exceeds 4000, the flow becomes turbulent[28]. The capillaries have a low Reynolds number due to their reduced radius and little velocity relative to other vessels, leading to laminar rather than turbulent flow [29].

### 1.3.5 WALL TENSION

Irrespective of location, blood pressure correlates with the tension of the vessel wall as per Young–Laplace's equation:

$$\sigma_\theta = \frac{Pr}{t} \quad (17)$$

In this context,  $P$  represents blood pressure,  $t$  is the wall thickness,  $r$  is the internal radius of the vessel, and  $\sigma_\theta$  is the hoop stress, or cylinder stress. For the thin-walled assumption to hold, the vessel's wall thickness should be no more than about one-tenth (or sometimes one-twentieth) of its radius. Hoop stress refers to the average force exerted around the cylinder's circumference, perpendicular to both the axis and the radius.

$$\sigma_\theta = \frac{F}{tl} \quad (18)$$

$F$  stands for the circumferential force on a section of the cylinder wall,  $t$  is the radial thickness of the cylinder, and  $l$  is the axial length of the cylinder [22].

### 1.3.6 BLOOD PRESSURE

Circulation is primarily driven by the heart's pumping action. This action generates pulsed blood flow, which travels through arteries to the whole body and then returns to the heart. During each cardiac cycle, arterial blood pressure varies between systolic and diastolic pressure. In physiology, these values are often combined into a single value called the mean arterial pressure (MAP), calculated as follows:

$$MAP = DP + \frac{1}{3}PP \quad (19)$$

In this context, MAP stands for Mean Arterial Pressure, DP represents Diastolic blood pressure, and PP is Pulse pressure, which is the difference between systolic and diastolic pressure [30]. Changes in average blood pressure assist in moving blood through different regions of the circulatory system. The mean blood flow rate is determined by both blood pressure and resistance in the vessels. As blood flows from the heart through arteries and capillaries, pressure decreases because of energy loss from viscosity, with most of the pressure drop occurring in small arteries and arterioles. Gravity affects blood pressure through hydrostatic forces (like when standing), and factors such as venous valves, breathing, and muscle contractions also impact venous blood pressure. The relationship between pressure, resistance, and flow is expressed by the following equation:

$$Flow = \frac{pressure}{Resistance} \quad (20)$$

When applied to the circulatory system, we get:

$$CO = \frac{MAP - RAP}{SVR} \quad (21)$$

In this context, CO stands for cardiac output (measured in liters per minute, L/min), and MAP represents mean arterial pressure (measured in millimeters of mercury, mmHg), which is the average pressure of blood leaving the heart. RAP refers to right atrial pressure (measured in mmHg), which is the average pressure of blood returning to the heart. SVR denotes systemic vascular resistance (measured in mmHg \* min/L). A simplified version of this equation assumes that right atrial pressure is approximately:

$$CO \approx \frac{MAP}{SVR} \quad (22)$$

The ideal blood pressure in the brachial artery, where standard blood pressure cuffs measure pressure, is less than 120/80 mmHg. Other major arteries show similar blood pressure readings, indicating minimal differences among them. For example, the innominate artery averages 110/70 mmHg, the right subclavian artery averages 120/80 mmHg, and the abdominal aorta averages 110/70 mmHg. The consistent pressure in these arteries indicates that they act as a pressure reservoir for the blood they carry. As blood flows from the major arteries through the arterioles and capillaries, pressure gradually decreases. Blood is then pushed back to the heart via the venules and veins, with the help of muscles. The flow rate is determined by the resistance to blood flow at any given pressure drop. In healthy arteries, there is little to no resistance to blood flow. The diameter of the vessel is the main factor affecting resistance. Compared to

smaller vessels in the body, arteries have a much larger diameter (4 mm), resulting in less resistance [31]. The arm-leg blood pressure gradient is the difference in blood pressure readings between the arms and legs. It is usually less than 10 mmHg but can become higher in conditions such as aortic coarctation [32].

#### 1.4 RESEARCH OBJECTIVES

- To investigate the dynamics of bubble splitting across different flow regimes.
- To evaluate the impact of vessel branching on the splitting and path of bubbles.
- To assess the impact of non-Newtonian blood flow characteristics, including shear-thinning behavior, on bubble transport and deformation.
- To investigate bubble-wall interactions inside the artery.
- To explore the implications of bubble dynamics for biomedical applications, including targeted drug delivery and the minimizing risks associated with embolism.

# CHAPTER 2

## LITERATURE REVIEW

### 2.1 INTRODUCTION:

Studies have investigated the mechanics of bubble transit and division in blood flow through bifurcations and stenoses, underscoring their prospective implications in gas embolotherapy, targeted drug administration, and diagnostic imaging. The intricate behavior of bubbles in these situations is crucial for guaranteeing the safety and effectiveness of these therapies.

This literature review offers an extensive examination of bubble transit and splitting dynamics in blood flow, concentrating particularly on bifurcations and stenoses. Critical factors under examination encompass the impact of bifurcation angles, stenosis geometry, non-Newtonian properties of blood flow, and the dynamics of perfluorocarbon (PFC) bubbles. The paper also analyzes the stability of gas bubbles and the contribution of numerical simulation models to enhancing our comprehension of these phenomena.

This review synthesizes recent research findings to identify key elements influencing bubble behavior in vascular environments and to highlight existing knowledge gaps. These insights will guide future research and enhance the formulation of advanced medicinal and diagnostic approaches.

### 2.2 BUBBLE DYNAMICS IN THERAPEUTIC APPLICATIONS

Bento et al. (2020) studied how air bubbles impact local hematocrit levels in a narrow channel network with consecutive branches. The research indicated that air- bubbles substantially influence local hematocrit, reducing it downstream and elevating it upstream. Over time, Hct stabilizes independent of bubble impact. Bifurcations generate bubbles of diverse dimensions, resulting in an uneven hematocrit distribution. The division of bubbles at bifurcations influences red blood cell distribution, potentially leading to ischemia from gas embolisms. These findings highlight how air bubbles influence blood flow and the distribution of cells in microcirculation and medical devices [33].

Wang et al. (2018) developed a numerical model to simulate microbubble behavior in an elastic micro-vessel under ultrasonic waves. Using viscous flow theory and the boundary-element method, the model incorporates tissue elasticity through a pressure term at the fluid interface. The model was validated by comparing its results with Rayleigh-Plesset's equation for spherical bubbles, calculations for non-spherical acoustic bubbles, and experiments involving spark-generated bubbles in a rigid cylinder. The research examined bubble expansion, collapse, jetting, and vessel wall deformation, concluding that ultrasound-induced bubble oscillations increase membrane permeability for drug administration and that vessel wall deformation is influenced by ultrasound amplitude and vessel radius [34].

Mukundakrishnan et al. (2008) created a mathematical model to study the motion of a symmetric bubble with a defined size within an artery, offering valuable insights into vascular bubble dynamics. Their key findings showed that at a steady state, the bubble's interface is closest to the endothelial wall in small arteries ( $Re=0.2$ ), with increasing distances in larger arteries ( $Re=2$ ) and small arteries at  $Re=200$ . A recirculation vortex near the bubble's trailing edge generates significant shear stress gradients on the endothelial wall, particularly in arterioles. Bubble residence time is longest in small arterioles ( $Re=0.2$ ), shorter in small arteries ( $Re=200$ ), and shortest in larger arterioles ( $Re=2$ ). Gravity's effect on bubble movement in small arteries and arterioles was found to be minimal, aligning with experimental data [35].

Kripfgans et al. (2005) investigated the efficacy of Acoustic Droplet Vaporization (ADV) for tumor therapy by blockage and subsequent necrosis. In the study, New Zealand White rabbits were put under anesthesia, and their left kidney was surgically exposed. Filtered droplet emulsions were injected into the left heart while the renal artery was insonified. Results showed a maximum 90% decrease in regional blood flow in the treated area, with an average 70% reduction in organ perfusion using ADV. In contrast, the untreated kidney experienced a maximum regional blood flow reduction of 18%. ADV-induced image-based hyper echogenicity persisted for approximately 90 minutes, during which cortical perfusion decreased by 60% for over an hour. These findings indicate that ADV may be useful for tumor treatment through ischemia necrosis and could enhance existing radiofrequency tissue ablation treatments by reducing heat loss due to vascular cooling [36].

Yang (1971) studied how gas bubbles behave in whole blood and plasma, focusing on the effects of surface tension and diffusion. The research indicated that, when disregarding surface tension, the diffusion and radius-time relationship for dissolving bubbles depend on four

dimensionless parameters. When surface tension is taken into account, these transform into functions of seven dimensionless parameters. Numerical integration indicated that the duration for a gas bubble to dissolve is affected by the reaction rate constant and the gas density. The study emphasized the significance of surface tension in reducing the duration of full dissolution[37].

Ye and Bull (2004) created a computational model to investigate microscale bubble dynamics in gas embolotherapy. The model replicates the acoustic vaporization of liquid perfluorocarbon droplets to generate bubbles that obstruct tumor blood flow. The research evaluated the likelihood of flow-induced wall stresses causing damage to vessels during vaporization by manipulating parameters such as Reynolds, Weber, and Strouhal numbers, inertial energy, and starting droplet size. The results indicated that wall pressure peaks during the initial phase of bubble expansion, but maximum wall shear stress is observed subsequently. Reduced initial bubble diameters lead to diminished wall tensions, hence decreasing the likelihood of endothelial injury [38].

### 2.3 THE BEHAVIOR OF BUBBLES IN HEMODYNAMIC FLOW

Nagargoje and Gupta (2020) performed a numerical analysis of bubble dynamics in bifurcating tubes to improve gas embolotherapy for cancer treatment. The researchers utilized a two-dimensional artery model featuring symmetric bifurcation angles between  $30^\circ$  and  $120^\circ$ , applying the Volume of Fluid (VOF) approach to simulate the flow of perfluorocarbon (PFC) bubbles in blood-filled capillaries. Their simulations demonstrated that at elevated capillary numbers ( $Ca = 0.0231$ ), bubbles divided uniformly at all bifurcating angles. At lower capillary numbers, that is,  $Ca = 0.00231$  and elevated bifurcating angles (where  $\alpha$  and  $\beta$  were  $60^\circ$ ), bubbles failed to divide and were directed into one of the daughter arteries. The study highlighted the critical role of the capillary number ( $Ca$ ) and bifurcation angle in bubble-splitting behavior, key factors in improving the effectiveness of gas embolotherapy [39].

Qamar et al. (2017) conducted simulations to study how small bubbles move through branching blood vessels, aiming to improve gas embolotherapy for the treatment of cancer. They used the Volume of Fluid (VOF) method to model how gas bubbles split into arteries and arterioles. The simulations matched many observed phenomena, including bubble reversal. The study found that small bubbles, less than twice the vessel diameter, were unlikely to split under gravitational imbalance. Additionally, the maximum shear strains along the vessel walls decreased

significantly with higher Reynolds numbers. The shearing caused by vortices in the vicinity of bifurcation was identified as a potential cause of endothelial cell injury [40].

Valassis et al. (2012) examined microbubble transportation inside a bifurcated vascular network under pulsed flow to provide insights into gas embolotherapy and two-phase microfluidics. The research employed theoretical and experimental models to examine microbubble dynamics. The one-dimensional time-dependent hypothetical model was derived using a modified unsteady Bernoulli's equation that incorporates viscous and unsteady phenomena. The results demonstrated that the roll angle markedly affected the bubble's splitting ratio at every branching in the network. Notwithstanding the order one Womersley numbers, pulsatile flow resulted in little alterations to the overall splitting ratio in comparison to continuous flow. The study revealed that bubble trapping was influenced by the pulsating nature of blood flow, with a direct relationship between the splitting ratio and bubble length. The ability of bubbles to remain trapped in bifurcations after stabilizing holds promise for the effectiveness of gas embolotherapy in blocking blood flow to tumors. It also highlighted that bubbles in microfluidic devices can retain information in both stable and unstable conditions [41].

Samuel et al. (2012) performed an *in vivo* investigation to examine Acoustic Droplet Vaporization (ADV) and its impact on vascular occlusion. PFC droplets were introduced into the aortal arch and evaporated using ultrasound, utilizing rat cremaster muscle for microscopy. The results indicated that larger bubbles were trapped after capillary exposure (mean length of 76  $\mu\text{m}$ , mean diameter of 36  $\mu\text{m}$ ) in contrast to feeder vessel exposure (mean length of 25  $\mu\text{m}$ , mean diameter of 11  $\mu\text{m}$ ). Despite differences in size, the ratio of bubble length to hydraulic diameter remained consistent at  $2.11 \pm 0.65$ . The findings present the initial optical proof of targeted vascular blockage using ADV, establishing a foundation for the progression of gas embolotherapy [42].

Wong et al. (2011) examined the process of acoustic droplet vaporization (ADV) within a rigid tube at physiological temperature, employing an ultra-high-speed camera for detailed observation. This research, driven by gas embolotherapy, examined the development of microbubbles generated by ADV and introduced a 4 stage empirical growth graph. The findings indicated that viscous resistance attenuated microbubble oscillations, yet vaporization might still transpire during bubble expansion. The experimental model delineated bubble evolution into four phases: quick initial growth, slow steady growth, irregular growth, and final steady

growth. The results presented the inaugural experimental proof of bubble evolution resulting from ADV under physiological settings, which corresponded well with theoretical predictions [43].

Qamar et al. (2010) investigated acoustic droplet vaporization (ADV) in gas embolotherapy. The research introduced a model for bubble development from microdroplets within a stiff tube, juxtaposing the findings with experimental investigations. Employing ultra-high-speed photography, they examined bubble expansion ratios for initial droplet sizes between 10 and 20  $\mu\text{m}$  in radius. The findings indicated that viscous resistance mitigated bubble oscillations, yet vaporization might still transpire during bubble expansion. The research elucidated the velocity, pressure, and stress distribution in both flexible and rigid tubes, underscoring the need to comprehend ADV dynamics for therapeutic applications [44].

Carlson et al. (2010) performed three-dimensional numerical simulations employing Phase Field theory to examine the dynamics of droplets in a bifurcation channel under symmetrical outflow circumstances. Two separate flow conditions were identified as splitting and non-splitting. The transition between these states was influenced by the initial droplet size and the Capillary (Ca) number. The Rayleigh–Plateau's instability was recognized as the mechanism causing droplet fragmentation at the threshold between the different regimes. In the splitting regime, droplets generated a symmetric distribution in the daughter branches, but in the other regime, droplets migrated into a single branch, resulting in an asymmetric flow. The study emphasized the flow's sensitivity to disturbances and proposed additional investigations into tip shape, multiple droplet interactions, and wettability effects [45].

Calderon et al. (2010) used a boundary-element approach to study the passage of a semi-infinite gas bubble through a bifurcation in a microvessel. They found that the bubble's splitting ratio increased with higher driving bubble pressures but decreased with larger bifurcation angles. Viscous losses at the bifurcation substantially influenced bubble velocity. Although the reversal of the bubble was not distinctly observed, meniscus reversal and recirculation zones were identified, indicating potential reversal or stagnation for finite bubbles. The model computed velocity profiles, pressures, and stresses, indicating elevated pressures and wall shear stresses at the bifurcation carina and adjacent to the contact line. These findings elucidate the forces and strains that cells may encounter as a result of bubble motion, pertinent to gas embolotherapy and microfluidic devices [46].

Lo et al. (2007) examined the influence of pulse duration and contrast agents on the threshold for acoustic droplet vaporization (ADV). It was determined that augmenting pulsatile duration of 1.44 MHz reduced both acoustic droplet vaporization (ADV) and inertial cavitation (IC) thresholds. Repetitive pulsing produced an impact analogous to that of single pulses with comparable "on-times." The utilization of contrast compounds markedly diminished the ADV threshold, rendering routine ADV practicable at reduced input power and across diverse anatomical sites [47].

Eshpuniyani et al. (2005) examined bubble transport in a vascular bifurcation model to improve gas embolotherapy for cancer treatment. The research investigated the impact of gravity and flow on bubble division across several bifurcating angles. The results indicated that the splitting was relatively uniform at a zero-roll angle but grew increasingly heterogeneous with the rise in roll angle due to gravitational effects. Bubbles may adhere at secondary bifurcations or within second-generation daughter tubes, despite consistent flow rates. The results indicate that both flow and gravity are essential in influencing bubble transmission and that successive doses may effectively deliver emboli to channels not obstructed by the initial dose[48].

## 2.4 STABILITY OF BUBBLE

Hanwright et al. (2005) studied how stable gas bubbles are and how surfactants affect the transfer of mass at the interface. It emphasizes that insoluble surfactants enhance bubble stability by creating a compressed monolayer at the liquid-gas interface, so diminishing gas permeability. In contrast, soluble surfactants, even at elevated concentrations, exert negligible influence on interfacial mass transfer owing to their dynamic equilibrium of adsorption and desorption, which generates transient vacancies that allow gas molecules to traverse the contact. The review synthesizes previous research on surfactant effects and posits that processes of bubble stability are predominantly influenced by the kind and behavior of surfactants. This knowledge is crucial for comprehending processes such as bubble dissolution, gas exchange, and the function of surfactants in many applications[49].

Hartunian and Sears (1957) posited that gas bubbles ascending in an inviscid fluid experience instability due to the interplay between surface tension and pressure. Meiron (1989) devised a numerical approach that demonstrated stability in the translation mode, hence contradicting their conclusions. Meiron's study identified spiraling solutions attributed to surface tension; however, these did not align with experimental results due to a significantly elevated phase

speed. G. K. Batchelor (1987) investigated the amplification of perturbations in ascending bubbles, proposing a relationship between the initial disturbance and the maximum survival value of  $R$ [50].

Meiron (1989) noted that in an inviscid fluid, ascending gas bubbles persisted, contrary to the forecasts of linear instability theories that accounted for pressure forces and surface tension. The study emphasized the deficiencies of a non-rotational model for the entire bubble while affirming the validity of predictions predicated on an irrotational flow pattern at the bubble's forefront[51].

In 1987, G. K. Batchelor investigated the amplification effects of perturbations on gas bubbles ascending through a liquid. Batchelor recognized the unpredictability of a bubble's rupture but suggested that it was possible to assess the total amplification of a localized breakdown. She suggested that there might be a link between the strength of the initial disturbance and the maximum value of the parameter  $R$  at which the bubble can remain stable [52].

Herrada et al. (2021) analyzed the stability of a bubble rising in a vertical capillary with an external flow. When a downward external flow opposed the buoyancy-driven rise of the bubble, it resulted in various bubble dynamics. Through steady-axisymmetric simulations, they delineated the multiplicity of solutions, presenting bifurcation diagrams that illustrate three steady-axisymmetric solution branches and two critical points. The linear analysis of global stability revealed that symmetry breaking resulted from three-dimensional instabilities characterized by an azimuthal wavenumber of  $|m| = 1$ . The results corroborated experimental and numerical observations, elucidating asymmetry in the bubble profile as the capillary number neared the critical value [53].

## 2.5 BUBBLE-CAPILLARY WALL INTERACTION

Podvin et al. (2008) experimented on the interaction of bubbles with sloped surfaces utilizing a model grounded in lubrication theory. They classified bubble motion into three categories based on wall inclination: sticking motion for angles less than  $10^\circ$ , sliding motion for angles between  $10^\circ$  and  $55^\circ$ , and repetitive bouncing for angles beyond  $55^\circ$ . The model precisely forecasted the timescale and rebound amplitude for inclinations below  $55^\circ$ – $60^\circ$ , but did not replicate minor fluctuations in tangential velocity resulting from significant interface deformations. For inclinations over  $55^\circ$ – $60^\circ$ , the model failed to replicate constant bouncing motion, presumably due to the lack of lift effects in the lubrication model [54].

Tihon et al. (2014) explored the movement of individual bubbles in rectangular channels with high aspect ratios, analyzing both tilted and upright positions with either still or upward-moving liquid. Wall shear stress was quantified using two-strip electro-diffusion probes, yielding insights into liquid film thickness and capillary waves at the posterior of the bubble. The research delineated three areas within the wall shear rate profile: bubble front, reversed film flow, and bubble awake. The laminar liquid co-flow increased the thickness of the liquid layer and guided the bubbles toward the centerline in inclined channels. The findings emphasized the necessity for additional research on the dynamics of bubble ascent and wall shear stress across different channel layouts [55].

Losi and Poesio (2016) performed a comprehensive study on the impact of viscosity on bubble dynamics in flat and mildly sloped pipelines. They employed image analysis and capacitance probes to quantify the drift velocity of air bubbles. Their findings indicated that heightened viscosity impeded bubble propagation and that the drift velocity varied as the bubble front advanced horizontally with the pipe. The results were examined utilizing two drift velocity closure equations, yielding a thorough comprehension of the influence of viscosity on bubble dynamics within the pipeline system [56].

Jeong and Park (2015) investigated how large bubbles behave when ascending near a wall under various boundary conditions, including no-slip, porous, and hydrophobic surfaces. They observed that the bubble's motion changes significantly based on the wall's boundary condition, especially when the initial distance between the bubble and the wall is small ( $s < 20$ ). On hydrophobic surfaces, entrapped air pockets facilitated the rapid establishment of a three-phase contact (TPC), resulting in the bubble sliding along the wall with considerable shape distortion. The study emphasized the significance of wall boundary conditions on bubble motion and proposed additional research into the dynamics of bubble ascent and wall shear stress across different configurations [57].

Zaruba et al. (2007) examine the dynamics of bubbles ascending in liquid flow adjacent to an upright wall. Two distinct types of motions were observed: For smaller bubbles, they moved by sliding along the wall, whereas larger bubbles bounced off the surface. A one-dimensional model was introduced to estimate bubble movement, focusing on the interaction between drag forces and other influencing forces. The numerical results were validated against high-speed video observations in a vertical acrylic duct, showing good agreement with experimental data.

The study highlights the need for further investigation into the dynamics of bouncing bubbles and the role of bubble-shape oscillations [58].

## 2.6 RESEARCH GAP

1. The movement of bubbles in bifurcating arteries, especially under different flow conditions and vessel structures, is not well understood. Studying this could provide valuable insights into how bubbles navigate complex blood vessels and their potential role in medical treatments.
2. While some research exists on bubble behavior in non-Newtonian fluids, there is limited focus on how non-Newtonian blood flow specifically affects PFC bubbles in bifurcating arteries. Exploring this could help create more realistic models of blood flow and improve our understanding of bubble transport.
3. Blood's unique rheological properties significantly influence its flow, but their exact impact on PFC bubble movement in bifurcating arteries remains unclear. Investigating this could shed light on how blood viscosity and elasticity affect bubble behavior, which is crucial for medical applications.
4. While PFC bubbles have been presented as a potential treatment for cancer through gas embolotherapy, there is a lack of research on the dynamics of PFC bubbles in blood flow. Researching how PFC bubbles behave in a blood flow might provide light on the viability and efficacy of utilizing PFC bubbles in gas embolotherapy.

# CHAPTER 3

## RESEARCH METHODOLOGY

### 3.1 NUMERICAL SIMULATION

This numerical experiment seeks to investigate the complex phenomena of 3D bifurcation, as well as the transition and splitting dynamics of gas bubbles. The finite volume technique (FVM) was employed to conduct a comprehensive examination of gas bubble behavior under diverse settings. The FVM is especially appropriate for this investigation since it effectively manages intricate geometries and boundary conditions, guaranteeing precise and dependable outcomes.

#### 3.1.1 DIMENSIONS OF THE MODEL

This research simulates bubble dynamics using a 3-dimensional artery model comprising a primary channel ( $d$ ) and two secondary arteries ( $d_1$  and  $d_2$ ). The diameters of the primary vessel and its two subsidiary vessels are 1 mm and 0.78 mm respectively. The bifurcation angle was maintained as symmetric, ensuring an equal degree between the daughter vessels concerning the horizontal axis. The simulations explored various bifurcation angles, denoted as  $(\alpha, \beta)$ , with examples including  $(\alpha=30^\circ, \beta=30^\circ)$ ,  $(\alpha=45^\circ, \beta=45^\circ)$ , and  $(\alpha=60^\circ, \beta=60^\circ)$ . Additionally, lengths  $L_1, L_2, L_3$ , equal to 4.5mm, 4mm and 4mm, were introduced to enhance the scope of the study. Non-Newtonian blood serves as the model for the primary phase, whilst a perfluorocarbon-PFC gas, characterized by a density of  $12 \text{ kg/m}^3$ , and a viscosity of  $2 \times 10^{-5} \text{ Pa.s}$  represents the secondary phase [59].

Blood flow was defined by the Carreau model with a time constant of 3.313 seconds, a power-law index ( $n$ ) of 0.3568, a zero shear viscosity of  $0.056 \text{ kg/m}\cdot\text{s}$ , and an infinite shear viscosity of  $0.00345 \text{ kg/m}\cdot\text{s}$  [60].

Geometry creation was facilitated using SolidWorks. After completing the sketches, they were converted into the surface plane and saved in the directory as Parasolid file format ( $x_t$ ). The resulting images showcase the configurations of bifurcation vessels at 60, 90, and 120 degrees. The subsequent images depict the configuration of the arterial model.

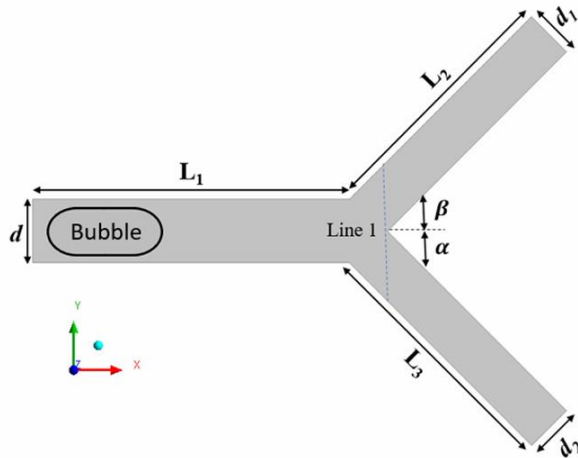


Figure 3-1: Schematic diagram of the bifurcation geometry [39].

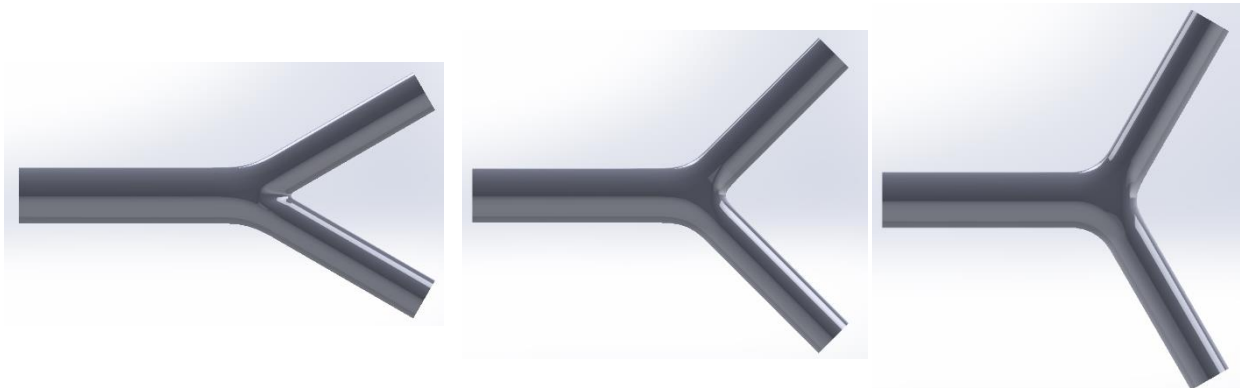


Figure 3-2: 3D model Geometries.

### 3.2 NUMERICAL MODELLING

The movement of PFC bubbles through a blood-filled arterial split represents a gas-liquid multiphase phenomenon. The model treats blood as a non-Newtonian fluid. The continuum surface force (CSF) based volume of fluid (VOF) technique is employed within the CFD software ANSYS Fluent 2024R1 to enable fluids to adhere to the gas-liquid interface. This method is favored for its accuracy, versatility, and reliability in resolving a singular set of momentum equations.

Following a mesh independence study, the arterial model was discretized using ANSYS and subsequently imported into ANSYS Fluent for further simulations. In the VOF formulation, blood constitutes the primary phase (liquid), whilst the PFC bubble represents the secondary phase (gas). The bubble is initially be patched  $y$  times the diameter of the mother vessel and  $x$  millimeters from the intake. The PFC bubble exhibits a surface tension of 0.05 N/m about the

blood. The outflow pressure boundary condition was established at gauge pressure. The PISO system will be employed for pressure-velocity coupling, utilizing a neighbor correction factor of 1, while pressure interpolation utilized the body force-weighted scheme. The terms in the momentum equations were discretized employing the QUICK technique. The Modified HRIC approach yielded an optimal boundary for interpolating the fluid interface. The unstable term was discretized utilizing a first-order implicit technique with non-iterative time advancement, and simulations proceeded with a time increment of  $1 \times 10^{-6}$  s.

### 3.3 GOVERNING EQUATIONS

Carreau Model :

$$\mu(\dot{\gamma}) = \mu_\infty + (\mu_0 - \mu_\infty)[1 + (\lambda\dot{\gamma})^2]^{\frac{n-1}{2}} \quad (24)$$

Volume fraction equation:

$$\frac{\partial \alpha G}{\partial t} + u \cdot \nabla \alpha G = 0 \quad (25)$$

At the interfacial cells, the mixture density and viscosity are calculated as the average values of the two phases, weighted by their volume fraction.

$$P = \alpha L \rho L + \alpha G \rho G \quad (26)$$

$$\mu = \alpha L \mu L + \alpha G \mu G \quad (27)$$

Continuity equation for 3D incompressible flow:

$$\frac{\partial u}{\partial x} + \frac{\partial v}{\partial y} + \frac{\partial w}{\partial z} = 0 \quad (28)$$

Navier-Stokes equation:

$$\rho \frac{dV}{dT} = -\nabla p + \rho g + \mu \nabla^2 V \quad (29)$$

Momentum conservation: In X-direction:

$$\begin{aligned} \frac{\partial}{\partial t} \rho u + \frac{\partial}{\partial x} \left[ \rho uu - \frac{4}{3} (\mu + \mu_T) \frac{\partial u}{\partial x} \right] + \frac{\partial}{\partial y} \left[ \rho uv - (\mu + \mu_T) \frac{\partial u}{\partial y} \right] + \frac{\partial}{\partial z} \left[ \rho uw - (\mu + \mu_T) \frac{\partial u}{\partial z} \right] = \\ - \frac{\partial p}{\partial x} - \frac{2}{3} \frac{\partial}{\partial x} \left( \mu \frac{\partial v}{\partial y} + \mu \frac{\partial w}{\partial z} \right) + \frac{\partial}{\partial x} \left[ (\mu + \mu_T) \frac{\partial v}{\partial x} + (\mu + \mu_T) \frac{\partial w}{\partial x} \right] \frac{\partial u}{\partial x} - \frac{2}{3} \frac{\partial}{\partial x} (\rho \kappa) \end{aligned} \quad (30)$$

Momentum conservation: In Y-direction:

$$\begin{aligned} \frac{\partial}{\partial t} \rho v + \frac{\partial}{\partial x} \left[ \rho vu - (\mu + \mu_T) \frac{\partial v}{\partial x} \right] + \frac{\partial}{\partial y} \left[ \rho vv - \frac{4}{3} (\mu + \mu_T) \frac{\partial u}{\partial y} \right] + \frac{\partial}{\partial z} \left[ \rho vw - (\mu + \mu_T) \frac{\partial u}{\partial z} \right] = \\ - \frac{\partial p}{\partial y} - \frac{2}{3} \frac{\partial}{\partial y} \left( \mu \frac{\partial u}{\partial x} + \mu \frac{\partial w}{\partial z} \right) + \frac{\partial}{\partial y} \left[ (\mu + \mu_T) \frac{\partial u}{\partial y} + (\mu + \mu_T) \frac{\partial w}{\partial y} \right] \frac{\partial u}{\partial y} - \frac{2}{3} \frac{\partial}{\partial y} (\rho \kappa) \end{aligned} \quad (31)$$

Momentum conservation: In Z-direction:

$$\begin{aligned} \frac{\partial}{\partial t} \rho w + \frac{\partial}{\partial x} \left[ \rho uw - \frac{4}{3} (\mu + \mu_T) \frac{\partial w}{\partial x} \right] + \frac{\partial}{\partial y} \left[ \rho vw - (\mu + \mu_T) \frac{\partial u}{\partial y} \right] + \frac{\partial}{\partial z} \left[ \rho ww - \frac{4}{3} (\mu + \mu_T) \frac{\partial w}{\partial z} \right] = \\ - \frac{\partial p}{\partial z} - \frac{2}{3} \frac{\partial}{\partial z} \left( \mu \frac{\partial u}{\partial x} + \mu \frac{\partial v}{\partial y} \right) + \frac{\partial}{\partial z} \left[ (\mu + \mu_T) \frac{\partial u}{\partial z} + (\mu + \mu_T) \frac{\partial v}{\partial z} \right] \frac{\partial u}{\partial z} - \frac{2}{3} \frac{\partial}{\partial z} (\rho \kappa) \end{aligned} \quad (32)$$

### 3.4 PROCEDURE FLOW DIAGRAM :

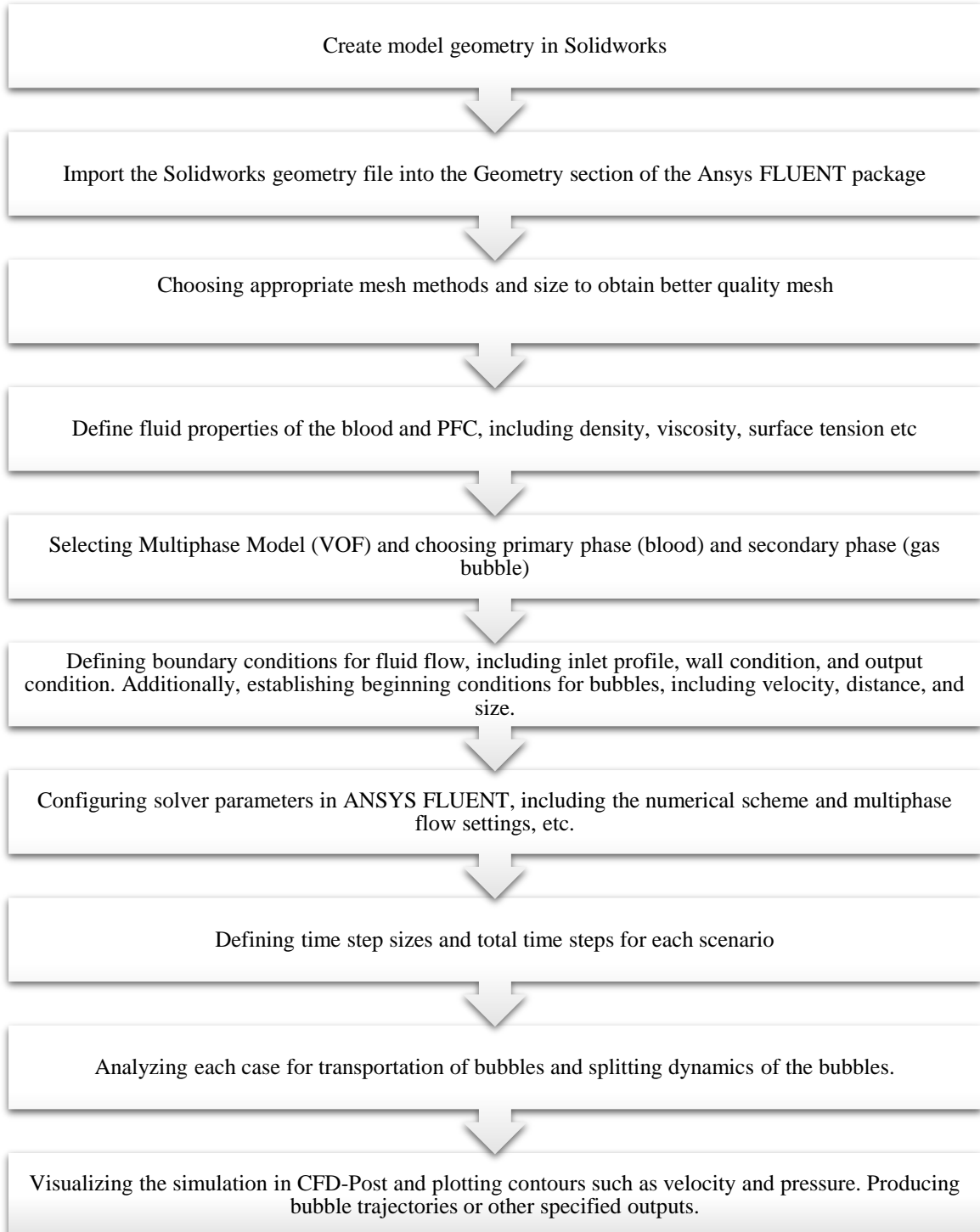


Figure 3-3 :Procedure flow diagram.

### 3.5 THESIS STRUCTURE DIAGRAM:

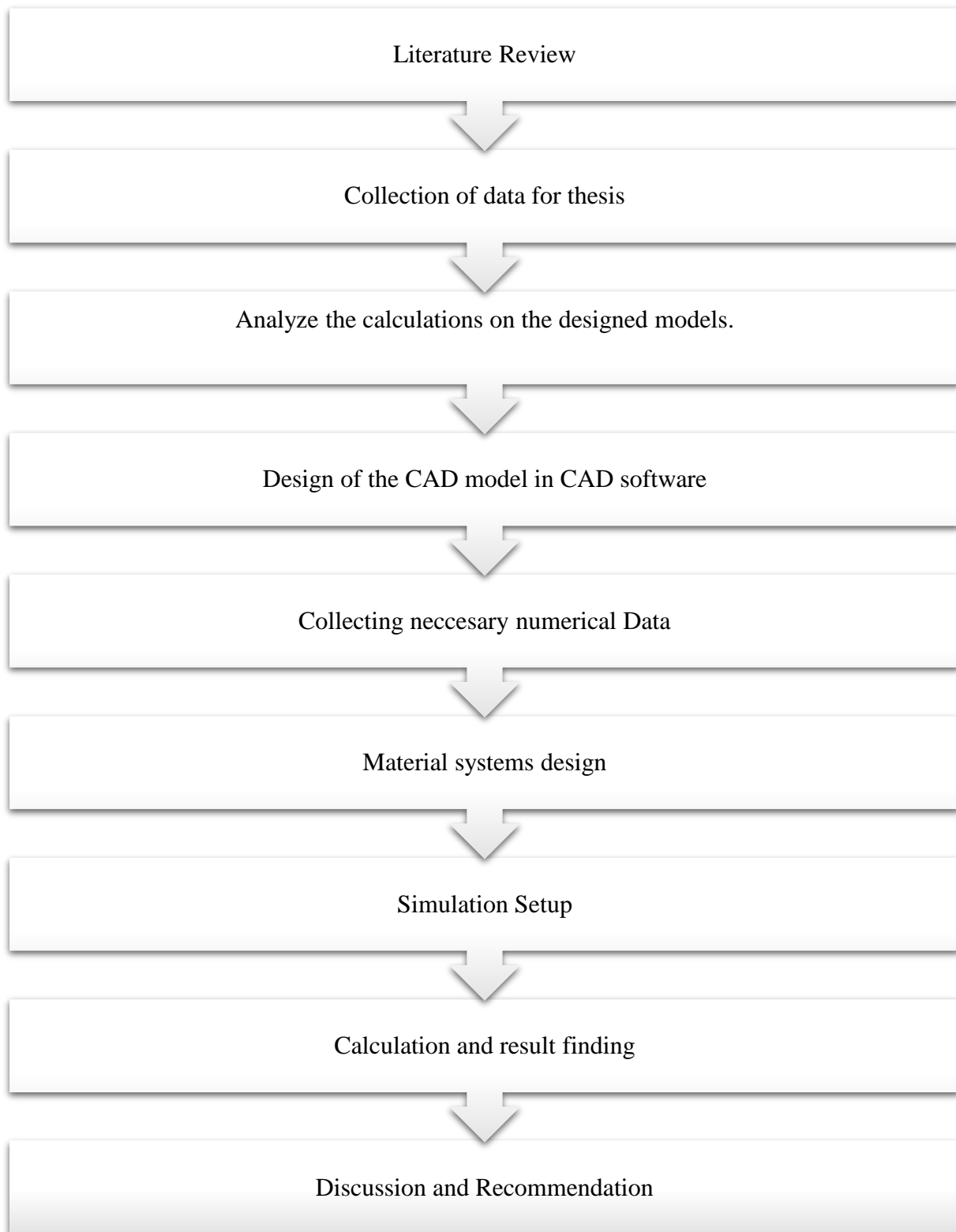


Figure 3-4: Thesis structure diagram

# CHAPTER 4

## 4.1 INTRODUCTION

This chapter takes a closer look at the simulation setup process in ANSYS Fluent, with a strong focus on the importance of meshing in achieving accurate and reliable results. It begins by walking through the meshing procedure, highlighting the critical role of the grid independence test, which ensures that the simulation results are not affected by further mesh refinement. Once the grid independence is confirmed, the mesh quality is carefully evaluated to make sure it meets acceptable standards.

With the meshing complete, the chapter then moves on to setting up the simulation environment. While Chapter 3 already introduced the basics of numerical modeling, this section builds on that foundation with a more practical perspective. It also outlines the boundary conditions and the overall solution setup, providing a clear and comprehensive guide to preparing the system for simulation.

## 4.2 MESHING

Meshing plays a vital role in computational fluid dynamics (CFD), as it directly impacts the accuracy of simulation results and the stability of solution convergence. ANSYS offers a dedicated meshing package within ANSYS Mechanical, designed to facilitate efficient and high-quality mesh generation. In this study, the geometry was initially created using SolidWorks and exported as a Parasolid file. This file was then imported into ANSYS, where the meshing process was carried out.

### 4.2.1 GRID GENERATION

Grid generation is a critical component of CFD simulations, as the accuracy and reliability of the solver's results depend heavily on how well the geometry is discretized. In this study, ANSYS Fluent Meshing was used to provide precise control over the mesh across the entire computational domain, with particular attention given to refining the mesh near boundary layers to capture flow behavior accurately. The meshing process was conducted in two main steps. First, the body sizing method was applied with an element size of 0.02mm to ensure fine resolution along critical regions. Following this, inflation was implemented by selecting the

wall with 10 layers of 0.04 mm in thickness in total. This meshing approach is applied uniformly across all geometry configurations to maintain consistency and adhere to the standards required for optimized and dependable simulations in ANSYS Fluent. The accompanying figures illustrate the resulting mesh configurations, highlighting the detailed and systematic meshing strategy employed.

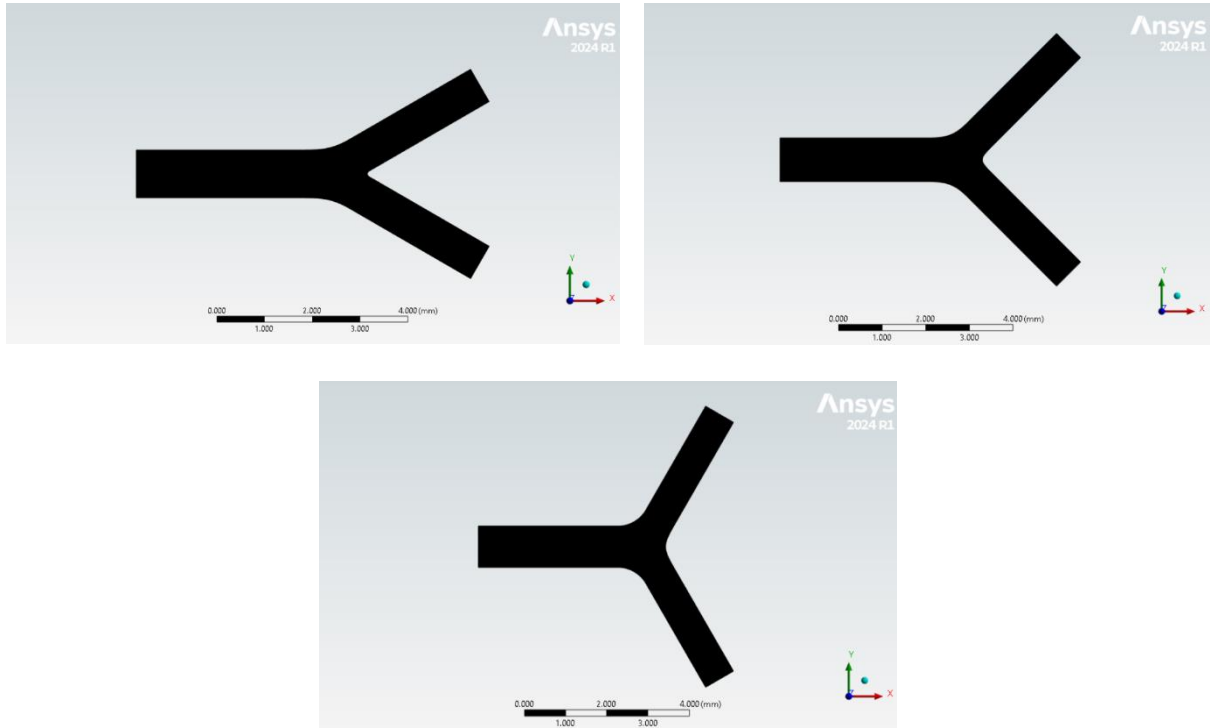


Figure 4-1: 60°, 90°, 120° bifurcation angles respectively.

#### 4.2.2 MESH INDEPENDENCE TEST:

The Mesh Independence Test was carried out to evaluate how different mesh resolutions affect the accuracy and stability of the CFD simulations. A range of mesh sizes was systematically tested to identify the level of refinement necessary for obtaining reliable results. All simulations were performed under consistent conditions, with uniform boundary conditions, identical geometry, and fixed solver settings.

Key output parameters—such as velocity profiles and pressure distributions—were analyzed to assess the sensitivity of the solution to mesh changes. The results showed that mesh sizes finer than 0.02mm had minimal impact on the simulation outcomes. In particular, the mesh with an element size of 0.02mm exhibited consistent and converged results, indicating the point at which mesh independence was achieved.

This analysis confirms that the selected mesh resolution is both accurate and efficient, ensuring dependable simulation results while making optimal use of computational resources. It provides a solid foundation for all subsequent simulations and analyses.

Table 4-1: Mesh Independence study

Body Sizing(mm)	Mesh Nodes	Mesh Elements	Pressure Outlet [Pa]	Velocity Outlet [ms <sup>-1</sup> ]
0.02	1857791	7500337	118.0519	0.3878954
0.021	1647730	6563652	118.2345	0.3892453
0.022	1470124	5782237	119.9503	0.3925322
0.025	1077405	4088802	138.8543	0.4235451
0.03	697598	2512226	151.5674	0.4348001

#### 4.2.3 MESH QUALITY

The quality of a generated mesh can be evaluated using several key metrics that directly influence the accuracy and stability of CFD simulations. The primary metrics considered in this study include:

- Element Quality
- Aspect Ratio
- Skewness
- Orthogonal Quality

Element Quality measures how closely the mesh elements approximate ideal shapes, with a value of 1 indicating a perfect element and 0 indicating a highly distorted or inaccurate one. The Aspect Ratio evaluates the ratio of the longest edge to the shortest, with values below 100 generally considered acceptable for most CFD applications. Skewness, which quantifies the deviation of mesh elements from their ideal shapes, is most favorable when close to zero, indicating highly uniform elements. Lastly, Orthogonal Quality reflects how well the mesh elements align with the flow direction and other elements, with values close to 1 representing excellent alignment and minimal numerical error.

The accompanying table provides a detailed summary of these mesh quality metrics across the various geometries used in the simulations. This evaluation ensures that the mesh structure is not only suitable for accurate computation but also promotes stable and convergent simulation behavior, thereby enhancing the overall reliability of the results.

Table 4-2: Mesh Quality.

		Element Quality (Average)	Aspect Ratio (Average)	Skewness (Average)	Orthogonal Quality (Average)
Acceptable Range		>0.3	Should not exceed 100	0.8 to 0 (Lower is better)	0.1 to 1.00 (higher is better)
Actual	60°	0.7425	2.9012	0.17394	0.82507
	90°	0.74632	2.9025	0.17373	0.82512
	120°	0.7453	2.9105	0.17465	0.82624

### 4.3 SIMULATION SETUP

This section outlines the systematic process employed to configure simulations in ANSYS Fluent. Six distinct geometries were simulated, each sharing a uniform setup protocol.

#### 4.3.1 INITIALIZATION

Upon initiating Fluent, a dedicated tab interface is revealed, encompassing essential options like Mesh and Solver. A preliminary mesh check is executed to ensure accuracy, followed by the specification of solver settings under the Solver tab, where a pressure-based type solver with transient settings is selected.

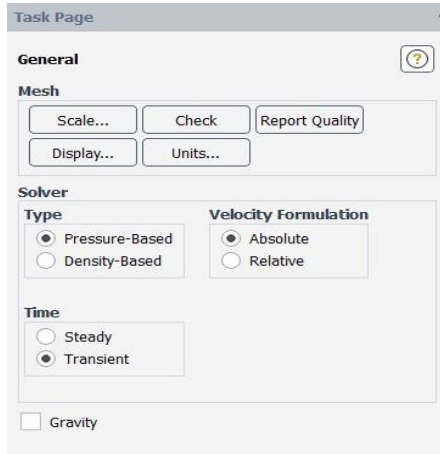


Figure 4-2: Transient Setup

#### 4.3.2 MODEL

#### CONFIGURATION

The selected model entails a laminar viscous approach for simplicity. The blood is modeled as non-Newtonian, and a perfluorocarbon (PFC) gas is utilized to represent the bubble, characterized by a viscosity of 2e-5 Pa.s and a density of 12 kg/m<sup>3</sup>.

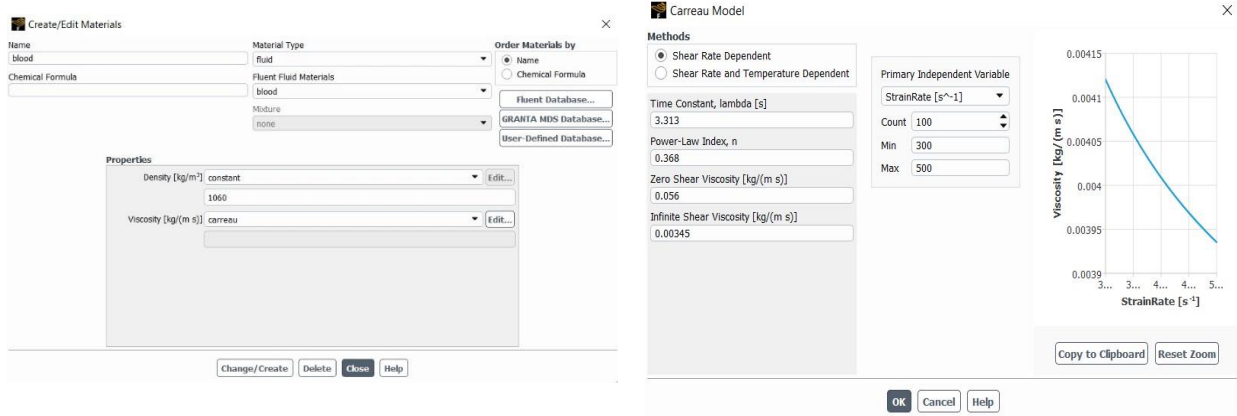


Figure 4-3: Materials Setup

### 4.3.3 MULTIPHASE MODEL

The multiphase aspect is activated, employing the Volume of Fluid (VOF) model. The Implicit Body Force formulation option is enabled, promoting convergence in pressure gradient and body forces within the momentum equations. The continuum surface force (CSF) based VOF technique is utilized for fluid-gas interface tracking. The PFC bubble exhibits a surface tension of 0.05 N/m relative to blood.

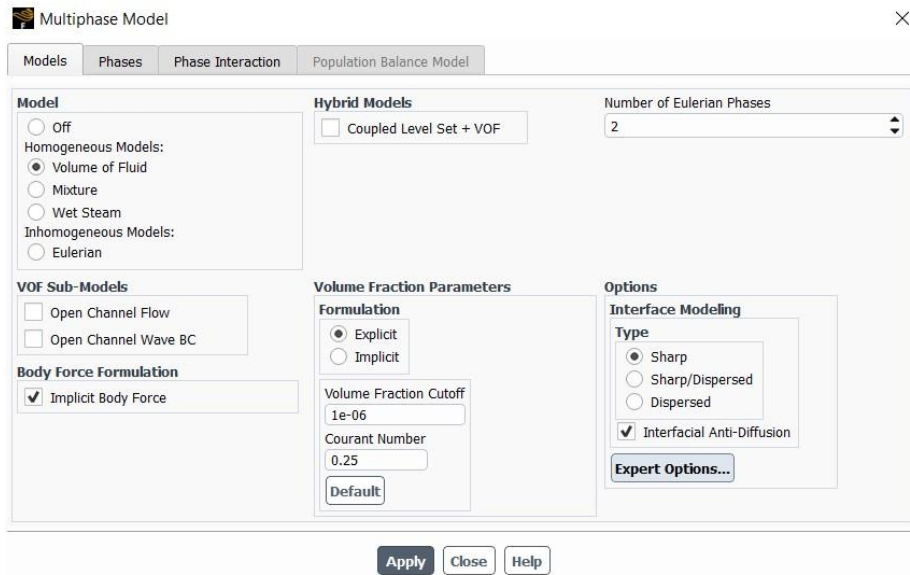


Figure 4-4: Multiphase Model Setup

### 4.3.4 BOUNDARY CONDITIONS

At the inlet, a fully developed velocity profile derived from a user defined function with

Reynold's number of 100 was introduced. The wall was treated as stationary with a no-slip boundary condition, and the outlet features a pressure boundary condition in gauge pressure terms.

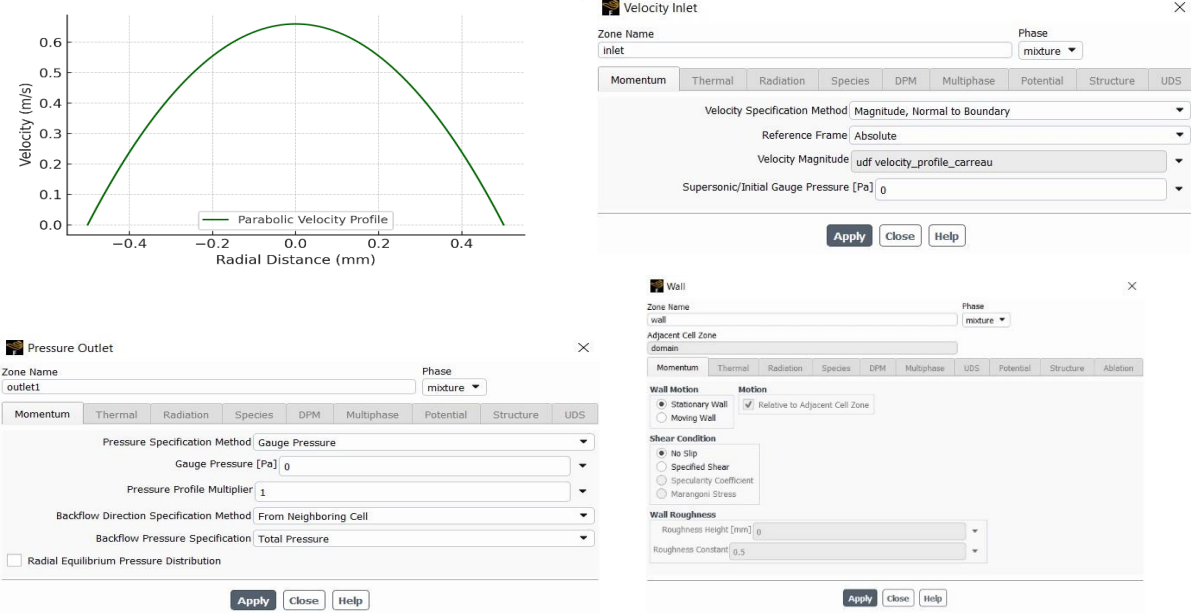


Figure 4-5: Fully developed parabolic velocity profile (Top-Left) & Boundary Conditions.

A recent study indicates that the splitting ratio remains unchanged between pulsatile and steady (constant) flow conditions [41]. So I have considered the inlet flow to be steady for all simulations.

#### 4.3.5 SOLUTION METHODS

The accuracy and computational efficiency of the simulation are strongly influenced by the selection of appropriate solution methods. In this study, pressure–velocity coupling is handled using the PISO (Pressure-Implicit with Splitting of Operators) scheme, which is well-regarded for its stability and relatively low computational cost. For pressure interpolation, the body force-weighted scheme is employed to enhance accuracy in flows influenced by gravitational or body forces. The QUICK (Quadratic Upstream Interpolation for Convective Kinematics) scheme is used for discretizing the momentum equations, offering higher-order accuracy in capturing flow variables. Additionally, to accurately track the fluid interface, the High-Resolution Interface Capturing (HRIC) scheme is implemented, ensuring sharp and precise resolution of multiphase boundaries.

#### 4.3.5.1 INITIALIZATION

The solution initializes from the inlet boundary condition, with the bubble region patched by setting the volume fraction to one. Taking a plane along XY of the 3D geometry, the volume fractions of PFC gas is shown in the blood domain.

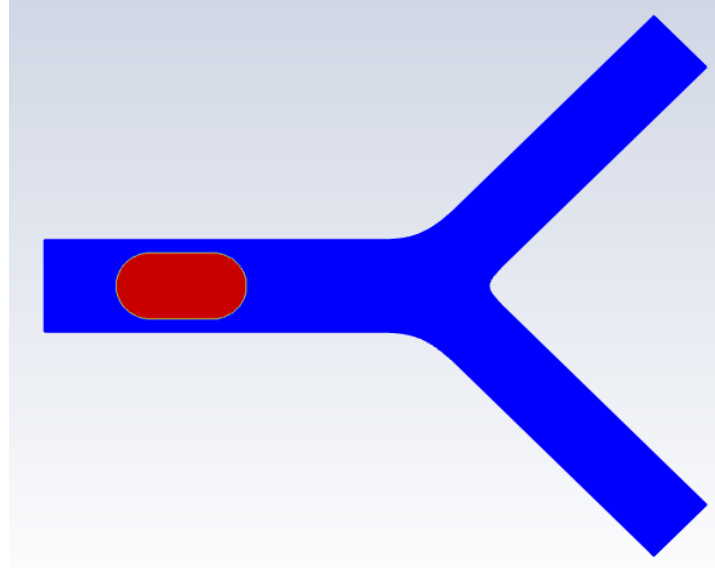


Figure 4-6: Initial Bubble Position.

#### 4.3.5.2 SOLUTION EXECUTION

Before initiating the simulation, a final system check was conducted, incorporating any recommendations provided by the ANSYS Fluent Solver to ensure numerical stability and consistency. The time step size was set to  $1 \times 10^{-6}$  seconds, and the total number of time steps is defined accordingly based on the desired simulation duration. Once all parameters are confirmed, the calculation is launched. The PISO (Pressure-Implicit with Splitting of Operators) scheme is chosen for its ability to handle transient simulations with large time steps and ensure better convergence for unsteady flows. Least Squares Cell Based method provides accurate gradient calculations, especially in unstructured meshes, improving the accuracy of the solution. The body force weighted option accounts for gravitational effects and other body forces, crucial for simulating blood flow in arteries.

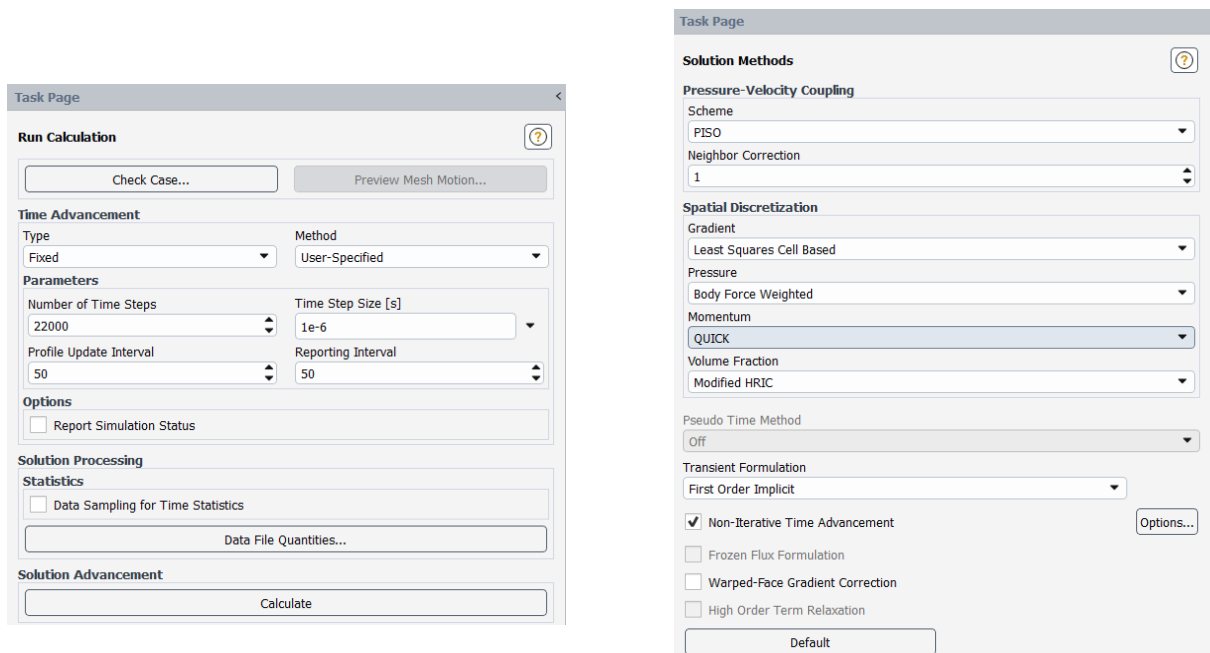


Figure 4-7: Solution Methods (left), Run Calculation (right).

The QUICK (Quadratic Upstream Interpolation for Convective Kinematics) scheme is used for momentum equations to reduce numerical diffusion and enhance solution accuracy in convection-dominated flows. The modified HRIC (High Resolution Interface Capturing) scheme is suitable for multiphase flows, providing accurate interface tracking between phases

# CHAPTER 5

## RESULTS AND DISCUSSION

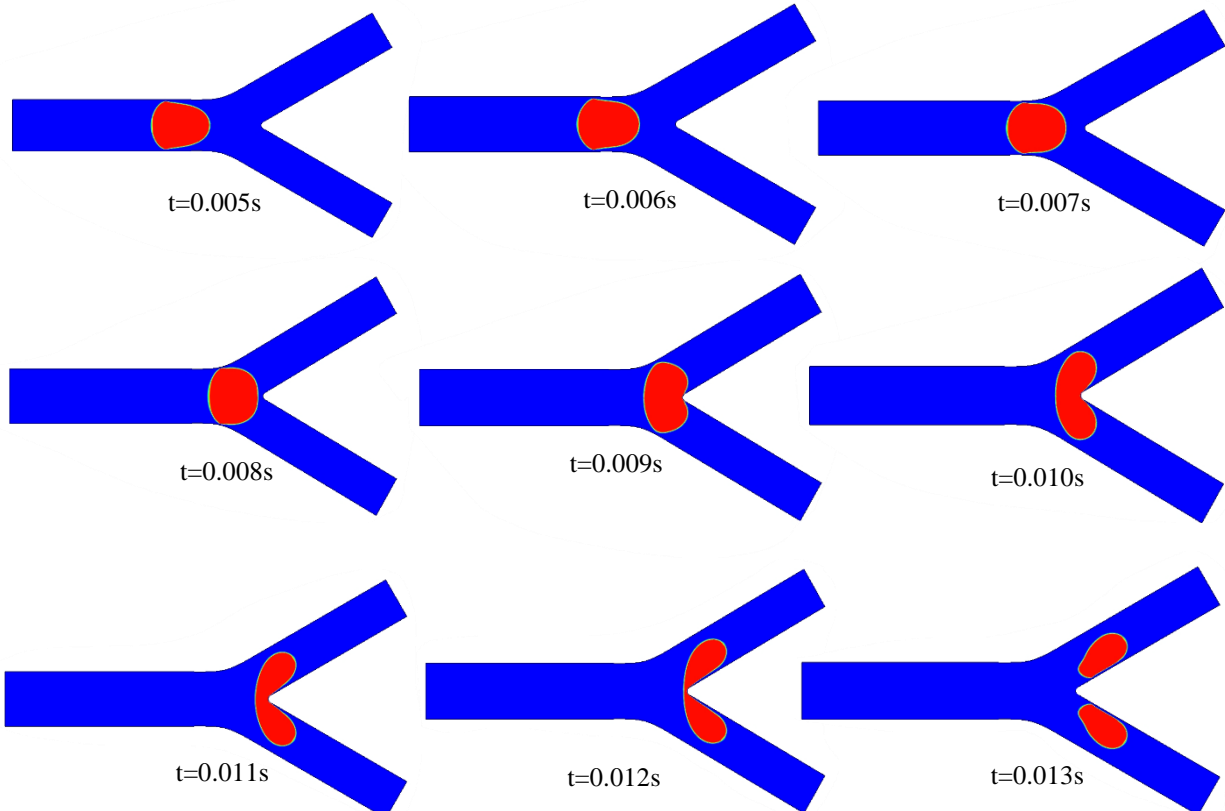
### 5.1 INTRODUCTION

After completing the simulations, the results are analyzed using CFD-Post, providing valuable insights into the flow behavior and performance characteristics captured during the simulation.

### 5.2 VESSELS WITH BIFURCATION ANGLES

Three types of bifurcation angles were considered to study and analyze the splitting behavior of a PFC gas bubble.

#### 5.2.1 60° BIFURCATION ANGLE



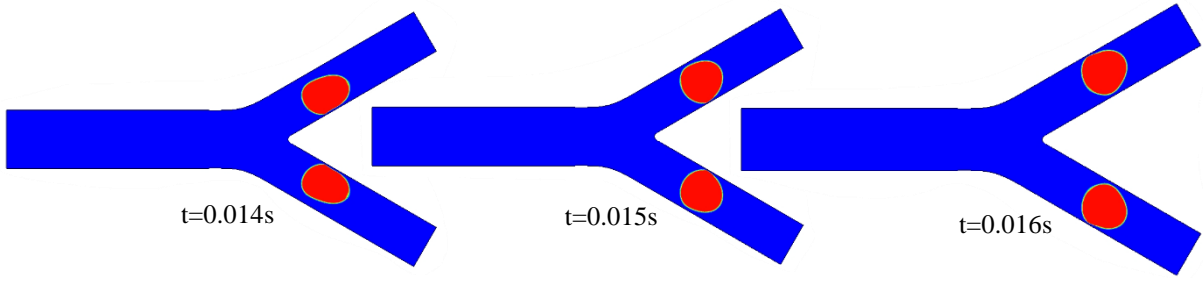
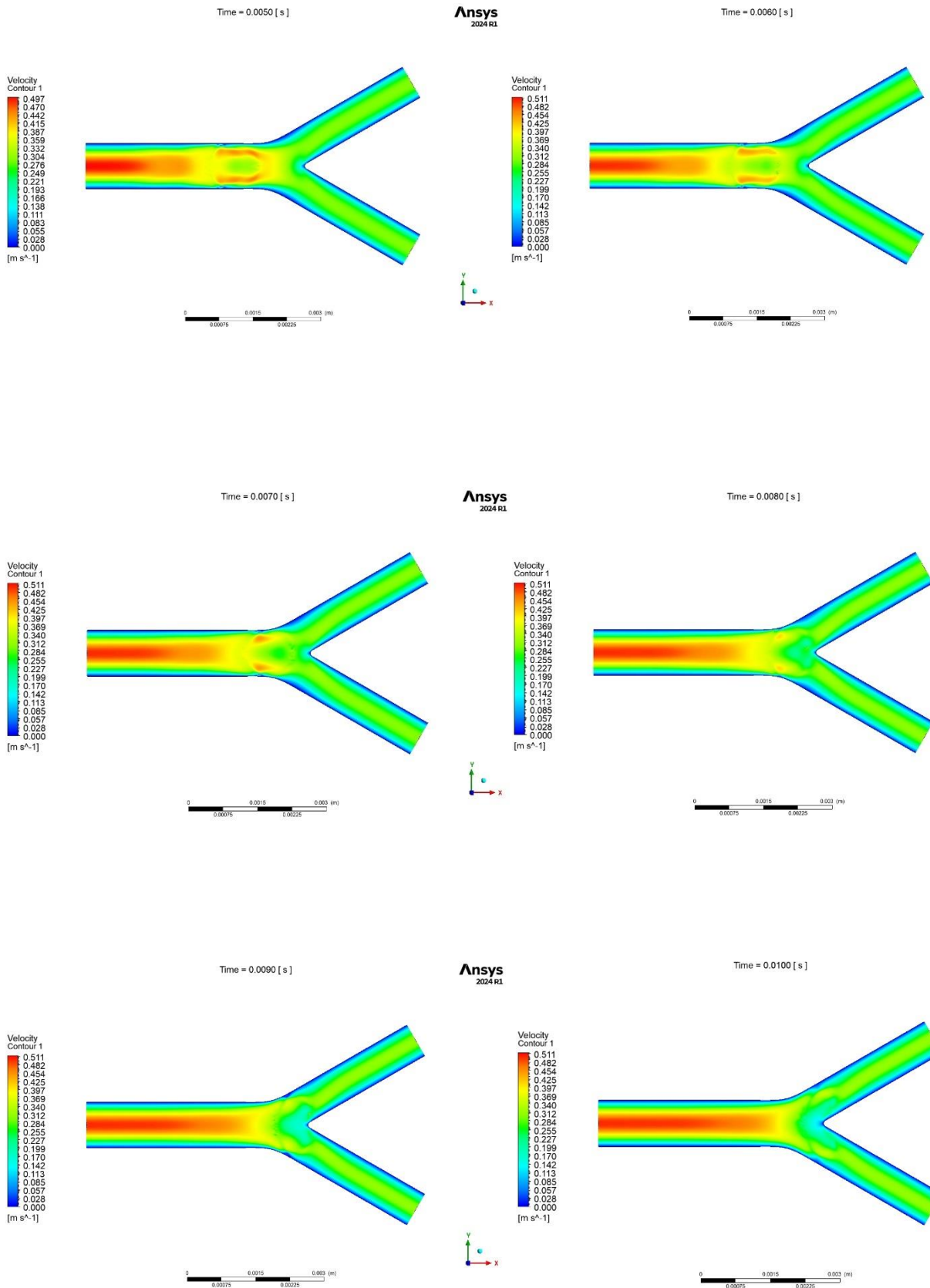


Figure 5-1:PFC bubble behavior at different time instances for 60° Bifurcation Vessel.

Figure 5-1 presents the temporal evolution of the gas bubble (PFC) volume fraction during its transport and splitting in a symmetric bifurcating artery of 60° bifurcation. The blue region represents blood, while the red region indicates the PFC gas bubble. The sequence of images illustrates the bubble's behavior over time, from its initial entry into the bifurcation region to its eventual division into the daughter vessels. Initially, the bubble enters the mother artery while maintaining a nearly symmetric and undeformed shape. As time progresses ( $t = 0.005$  s to  $t = 0.008$  s), the bubble migrates toward the bifurcation junction. During this phase, it begins to deform slightly, primarily at the trailing edge, which becomes increasingly concave due to interactions with the surrounding flow and wall shear. At around  $t = 0.009$  s, the bubble reaches the bifurcation point and experiences significant deformation. The frontal head of the bubble flattens as it encounters resistance from the vessel walls, while the trailing side begins to split symmetrically. This marks the onset of the bubble splitting process. By  $t = 0.012$  s, the bubble has clearly begun to divide into two lobes, each entering one of the daughter branches. The deformation intensifies at the bubble neck, leading to the formation of a thin connecting region between the two lobes. Eventually, this neck thins out completely, and the bubble pinches off into two daughter bubbles. Throughout the process, the symmetry of the bifurcation appears to support a uniform distribution of the bubble into both branches, with no significant bias in direction. This observation aligns with findings from previous studies, which noted that under steady flow conditions and symmetric geometries, the splitting ratio remains largely unaffected by transient flow characteristics. The interface between the blood and PFC bubble is well maintained during the motion, indicating a stable and sharp phase boundary, thanks to the use of a high-resolution interface capturing (HRIC) scheme. The resulting smooth splitting behavior suggests minimal interface fragmentation, and no satellite bubbles are observed in this simulation, due to the relatively low bifurcation angle and flow stability.



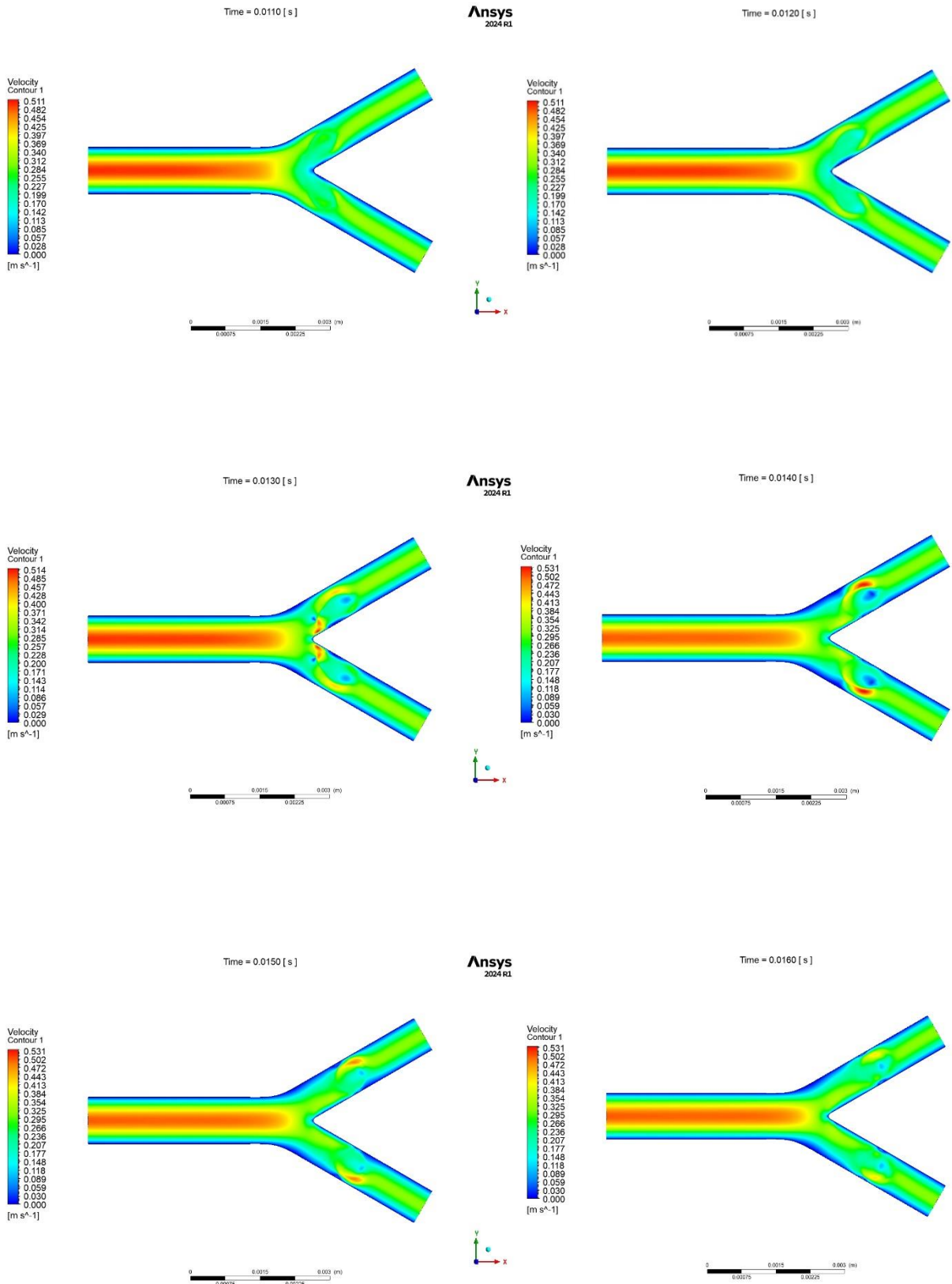


Figure 5-2: Velocity Contours at different time instances of 60° Bifurcation Vessel.

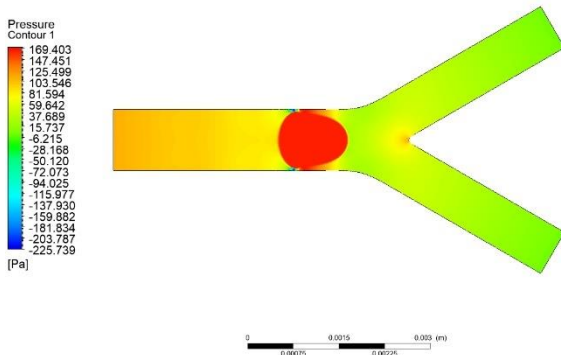
The velocity contours (Figure 5-2) reveal the dynamic behavior of a PFC gas bubble as it moves through a 60° arterial bifurcation at a Reynolds number of 100. In the early phase ( $t = 0.0050$ – $0.0100$  s), the bubble travels through the mother artery, where the flow maintains a classic parabolic velocity profile highest along the centerline (0.497–0.511 m/s) and tapering off near the walls. As the bubble nears the bifurcation, noticeable changes in its shape begin: the front edge flattens, and the rear develops a concave indentation. This indicates a slowing of flow near the bifurcation apex and the start of flow redistribution into the two daughter branches. Once the bubble interacts with the bifurcation region ( $t = 0.0110$ – $0.0140$  s), it acts as a significant obstruction, forcing the flow to split unevenly. High-velocity jets (0.413–0.531 m/s) develop along the inner walls of the daughter vessels, while stagnation zones (0.000–0.030 m/s) appear near the outer walls. At the same time, recirculating eddies form behind the bubble, with velocities ranging from 0.118 to 0.236 m/s. These vortices not only help maintain flow continuity but also add to the bubble's deformation. As the process continues, the bubble's trailing neck gradually thins, with flow speeds in this narrowing region dropping to 0.085–0.199 m/s—eventually leading to rupture and splitting.

Following this event ( $t = 0.0150$ – $0.0160$  s), the bubble separates into two asymmetrical daughter bubbles, influenced by the geometry of the 60° bifurcation. Flow in the daughter branches remains uneven, with stronger flow hugging the inner curves and weaker flow near the outer walls. Small satellite bubbles can be seen forming near the bifurcation apex—likely caused by thin film rupture as local velocities fall to as low as 0.000–0.057 m/s.

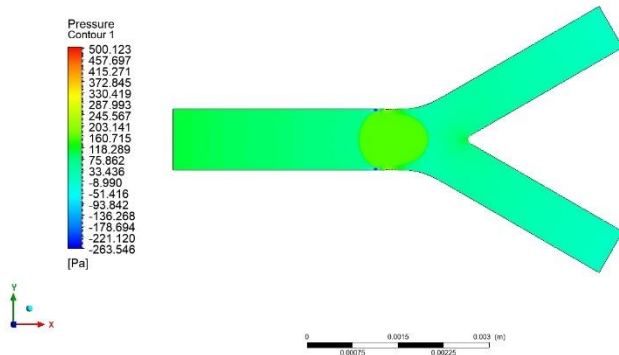
Overall, the 60° bifurcation introduces notable asymmetry into the flow, delaying the bubble's pinch-off and resulting in an uneven splitting pattern. These flow dynamics are important in understanding vascular transport behavior, as the presence of high-speed jets ( $\geq 0.413$  m/s) and stagnation regions ( $\leq 0.059$  m/s) may impose mechanical stress on the vessel walls, particularly at the bifurcation apex. Moreover, the presence of residual bubbles and persistent recirculation zones (0.148–0.295 m/s) post-splitting highlights the complexity of flow interactions, which may have implications for both therapeutic and diagnostic applications involving gas bubbles in blood vessels.

Time = 0.0050 [ s ]

Ansys  
2024 R1

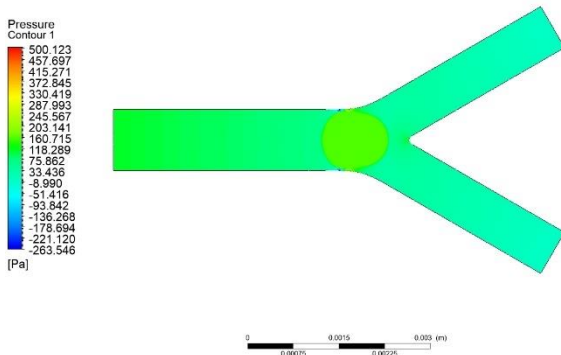


Time = 0.0060 [ s ]

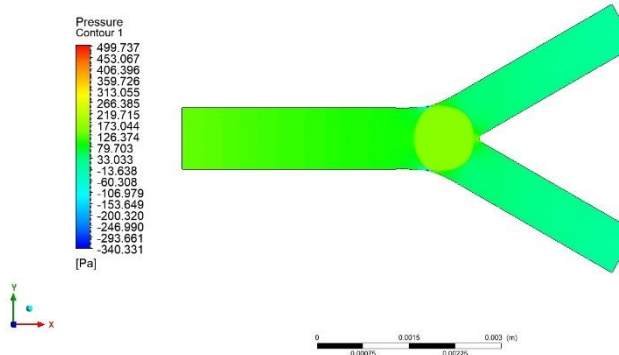


Time = 0.0070 [ s ]

Ansys  
2024 R1

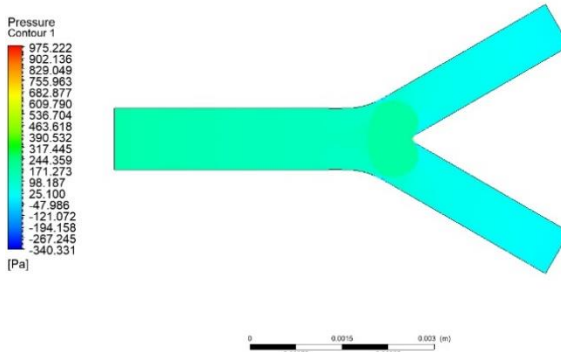


Time = 0.0080 [ s ]

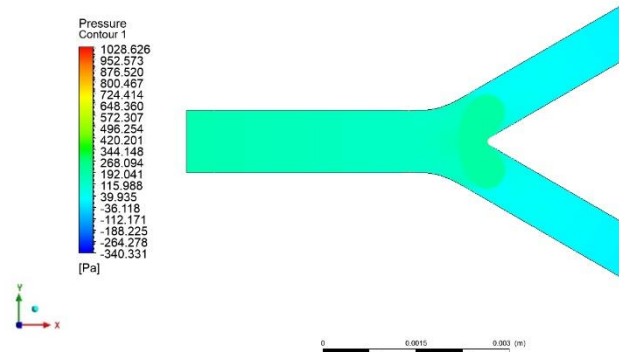


Time = 0.0090 [ s ]

Ansys  
2024 R1



Time = 0.0100 [ s ]



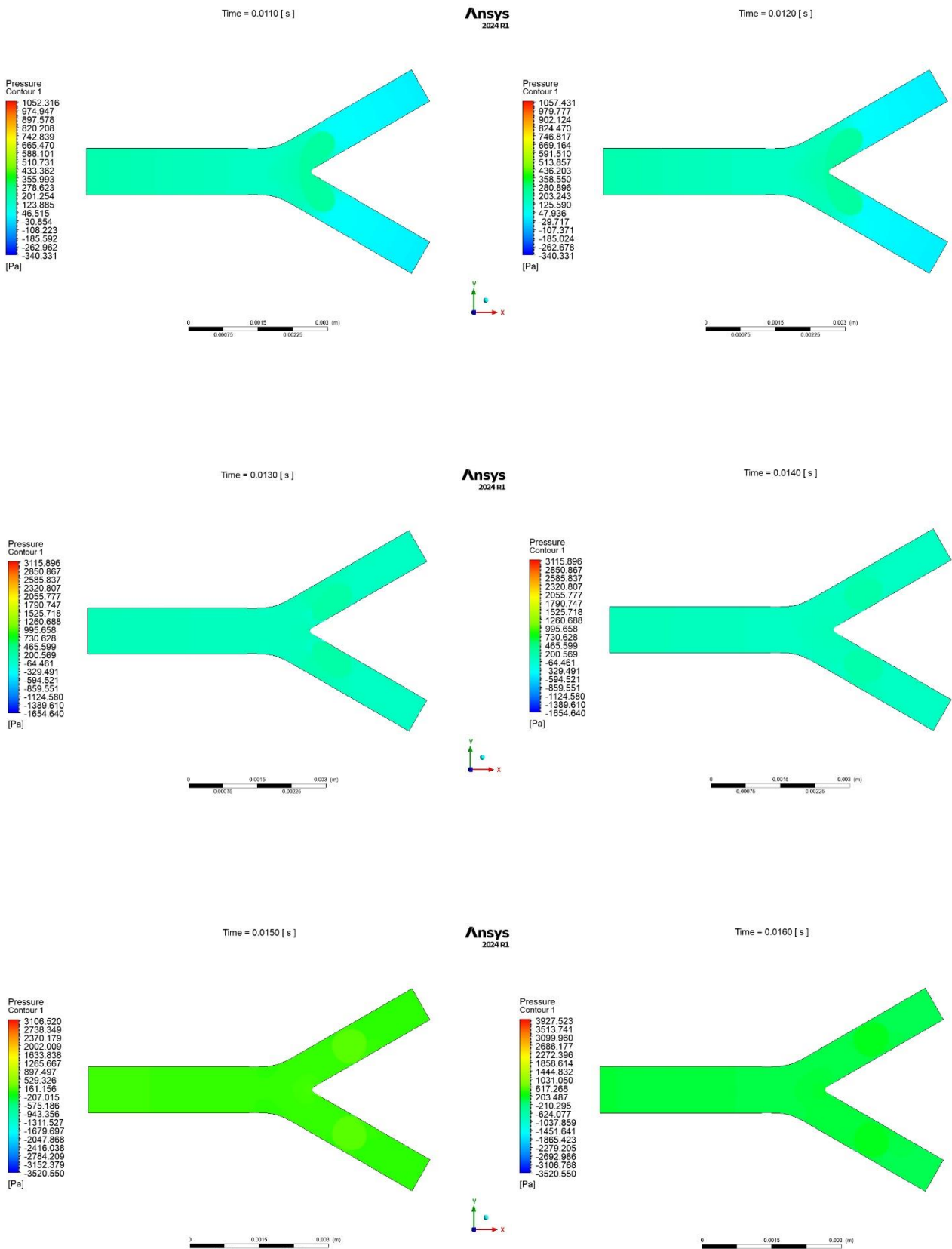


Figure 5-3: Pressure Contours at different time instances of 90° Bifurcation Vessel.

The pressure contours (Figure 5-3) show how the forces around the PFC gas bubble and blood

change as the bubble moves through a  $60^\circ$  arterial bifurcation. At the beginning (from 0.0050 to 0.0070 seconds), there's a noticeable difference in pressure from about -225 Pa behind the bubble to 500 Pa in front of it. This pressure difference acts like a push from behind and a pull from the front, driving the bubble forward.

As the bubble gets closer to the split in the artery (around 0.0080 to 0.0120 seconds), the pressure differences become much more intense. On the side where the bubble touches the vessel wall, pressures rise to over 1000 Pa, while on the opposite side, they drop to -340 Pa. This imbalance stretches the bubble, and because of the  $60^\circ$  angle, the deformation isn't even—it starts to pull more on one side than the other. The pressure difference across the bubble grows steadily during this phase, climbing from 840 Pa up to nearly 1400 Pa. The most dramatic moment comes when the bubble actually splits (between 0.0130 and 0.0160 seconds). Here, we see a sudden pressure spike of over 3900 Pa, which is nearly eight times higher than what we saw at the start. This kind of spike puts a lot of mechanical stress on the vessel walls. At the same time, extremely low-pressure zones as deep as -3520 Pa form between the two parts of the bubble. These low-pressure areas may lead to the creation of small extra bubbles, similar to what happens in cavitation. After the bubble has split, the pressure field starts to settle down, but not completely. The daughter branches of the artery don't behave the same: inner branches still show higher pressures (200–600 Pa), while the outer branches stay lower. The front sections of these new branches return to normal pressure quickly, but the central bifurcation area continues to have low pressure (between -2000 and -1000 Pa) for a while, which could affect how future bubbles behave if they follow. As the PFC bubble approaches and passes through the  $60^\circ$  arterial bifurcation, the surrounding flow field undergoes a series of noticeable changes, reflecting how the geometry shapes fluid motion over time.

From (*Figure 5-4*), in the early phase (0.0050–0.0070 s), the flow slows down as the bubble begins to obstruct the vessel. The axial component (U-velocity) shows a gradual decline, while the transverse flow (V-velocity) remains negligible indicating that the fluid is still primarily moving straight ahead. At this point, the bubble acts more as a moving blockage than a splitter, gently decelerating the flow without yet forcing any major redirection.

Things start to change as the bubble reaches the bifurcation apex (0.0080–0.0100 s). Here, the u-velocity drops to zero at the stagnation point right in front of the bubble, showing that the fluid momentarily comes to a halt before deciding where to go. Meanwhile, the v-velocity begins to rise on both sides, signaling that the fluid is now being diverted laterally into the

branches. This marks a turning point where the bubble and bifurcation together disrupt the flow and push it outward in two directions.

The splitting phase (0.0110–0.0130 s) brings the most dramatic shifts. The u-velocity suddenly splits rising sharply along the inner walls of the daughter vessels (reaching up to 0.5 m/s), while small areas near the outer walls show signs of backflow (as low as 0.0009 m/s). At the same time, the v-velocity peaks, especially at 0.0120 s, right when the bubble's neck is at its thinnest. This moment captures the full impact of the pinch-off: the pressure differences are at their highest, pushing the fluid strongly sideways and contributing to the bubble's final split.

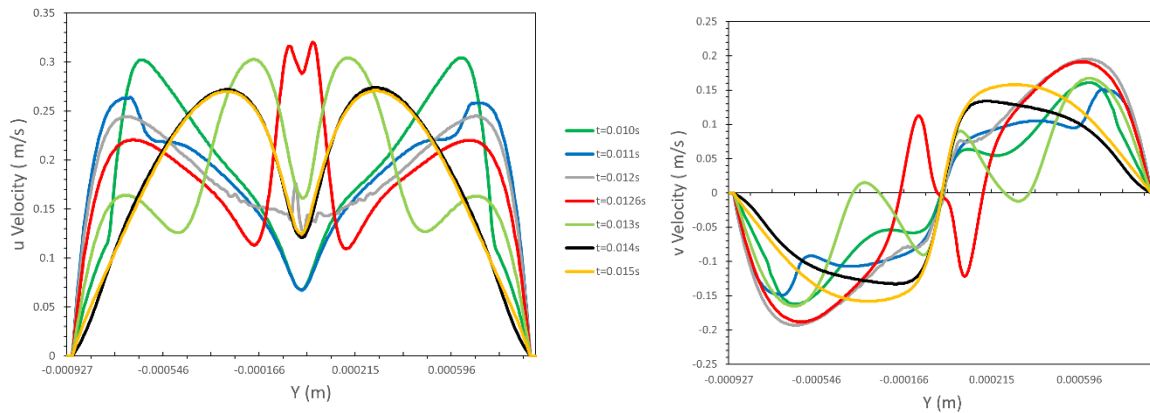
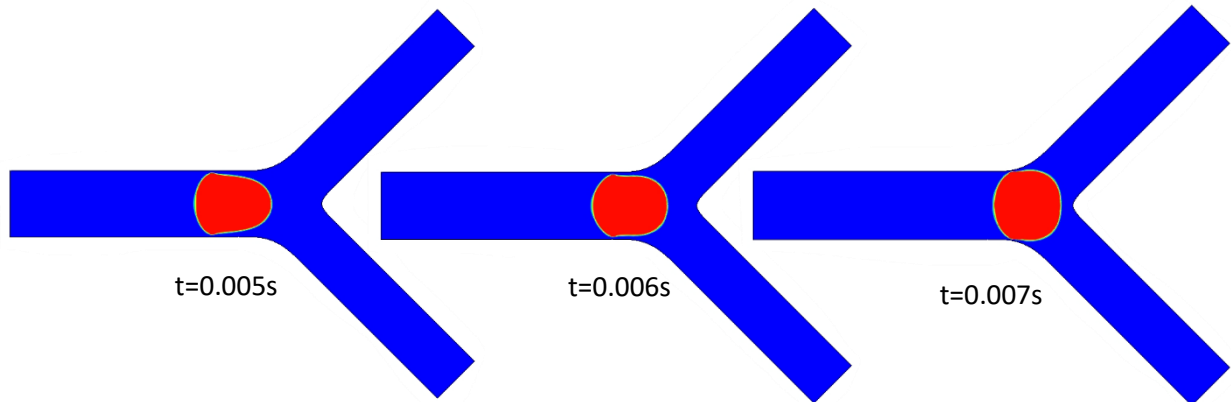


Figure 5-4: Velocity-u and Velocity-v Profiles of 60° Bifurcation Vessel.

### 5.2.2 90° BIFURCATION ANGLE



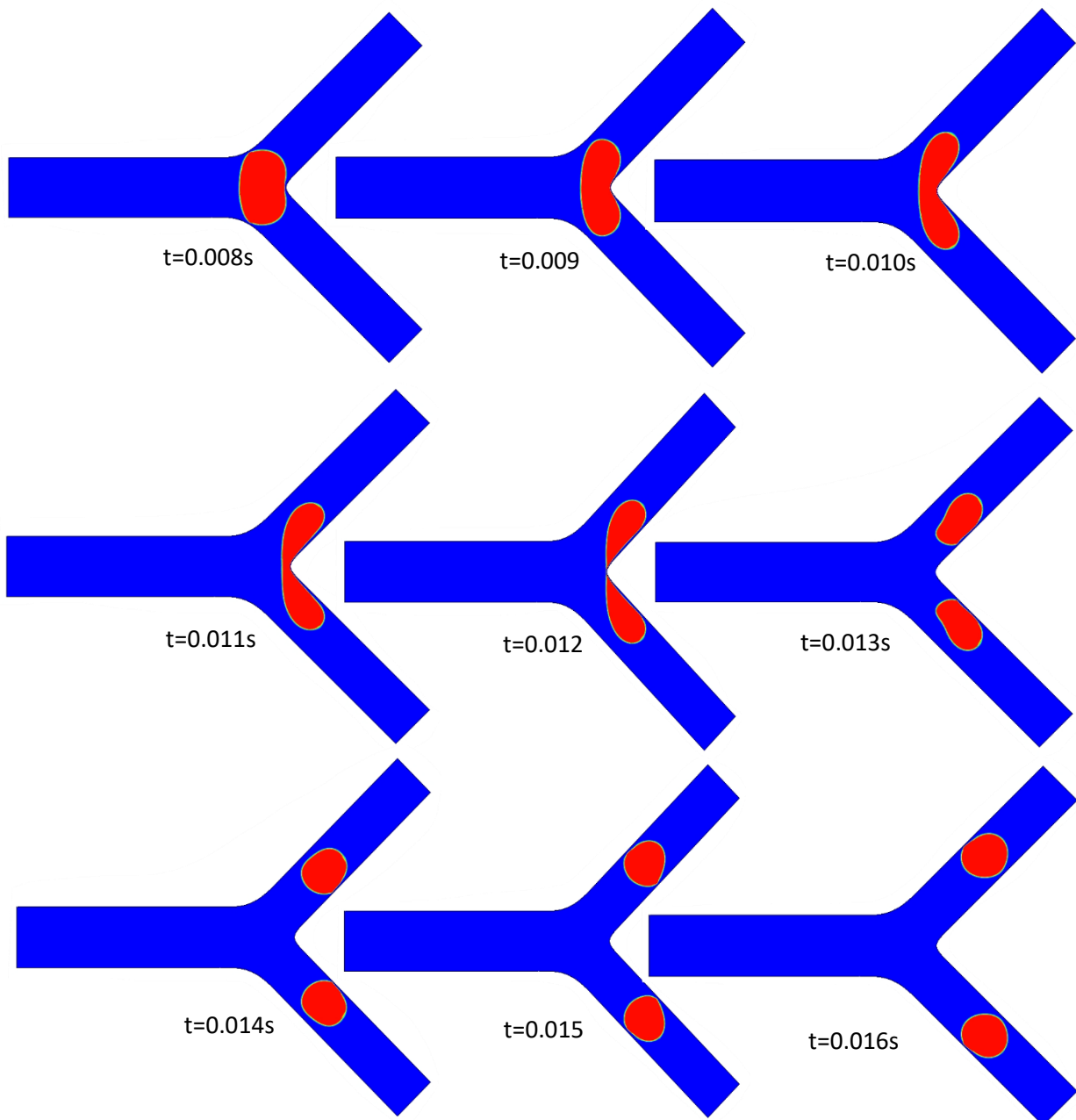
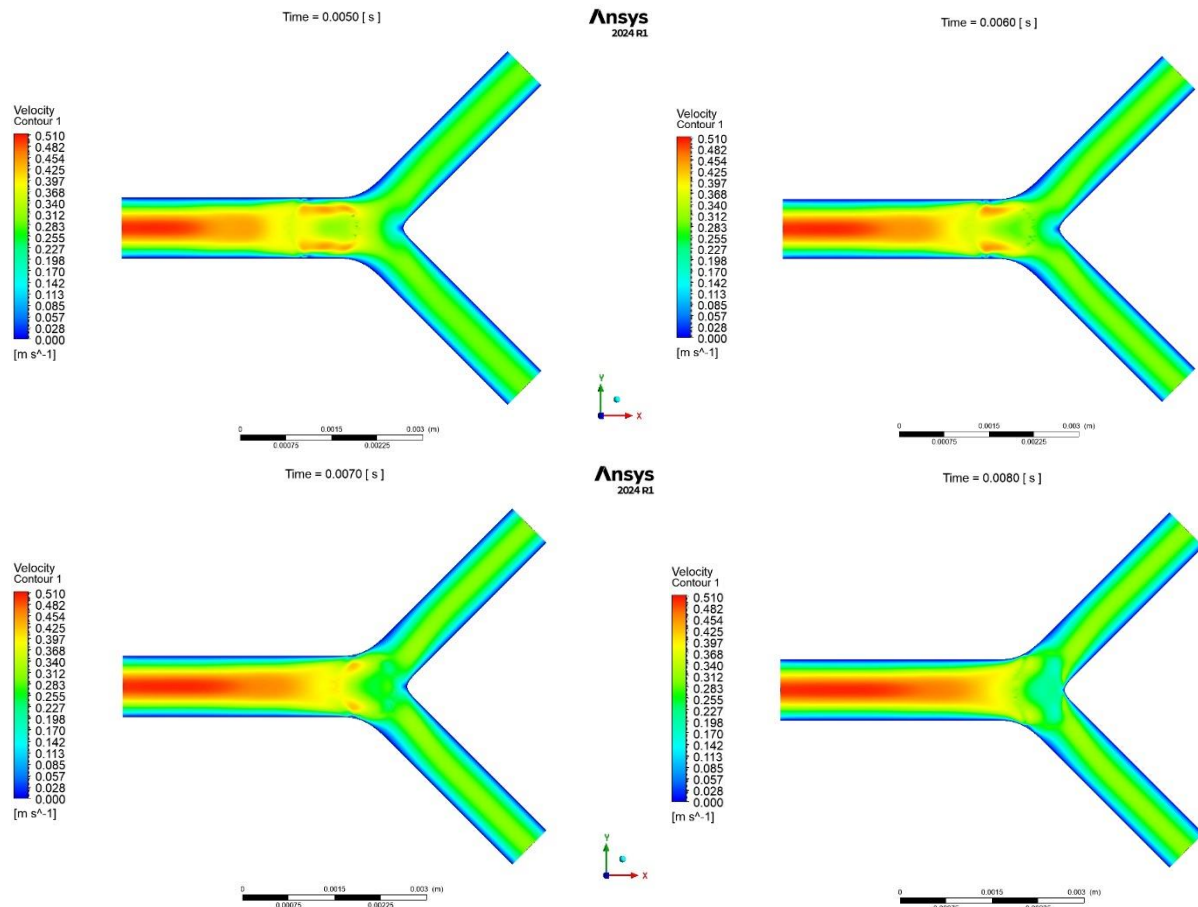


Figure 5-5: PFC bubble behavior at different time instances for 90° Bifurcation Vessel.

Figure 5-5 captures how the PFC gas bubble behaves as it moves through a 90° bifurcation and compared to the 60° case, the differences are quite striking. In the early moments ( $t = 0.005 - 0.008$  s), the bubble enters the mother vessel fairly symmetrically, much like in the 60° scenario. But as it nears the sharper 90° junction, the bubble begins to deform more noticeably. Although both cases show the bubble developing a concave trailing edge due to shear forces, the 90° bifurcation causes the front of the bubble to flatten more dramatically. This is especially

clear at around  $t = 0.009$  s, where the frontal shape is visibly compressed compared to the smoother, rounder profile seen in the  $60^\circ$  case. When the bubble starts to split ( $t = 0.011\text{--}0.016$  s), the process unfolds much more abruptly in the  $90^\circ$  geometry. The neck connecting the two sides of the bubble narrows quickly, driven by stronger resistance and sharper flow redirection. In contrast, the  $60^\circ$  bifurcation allows the neck to thin more gradually and evenly over time. Even though the  $90^\circ$  bubble still divides fairly symmetrically, there are small hints of uneven flow in the daughter vessels—likely a result of the more sudden pinch-off. The  $60^\circ$  case, with its gentler bend, promotes a more balanced and controlled splitting process. Despite these differences, both cases show stable gas-liquid interfaces throughout the simulation. There's no evidence of satellite bubble formation in either, which suggests that the bubble remains intact during its journey through both geometries. Still, it's clear that the  $90^\circ$  bifurcation leads to

faster, more intense deformation and speeds up the pinch-off process.



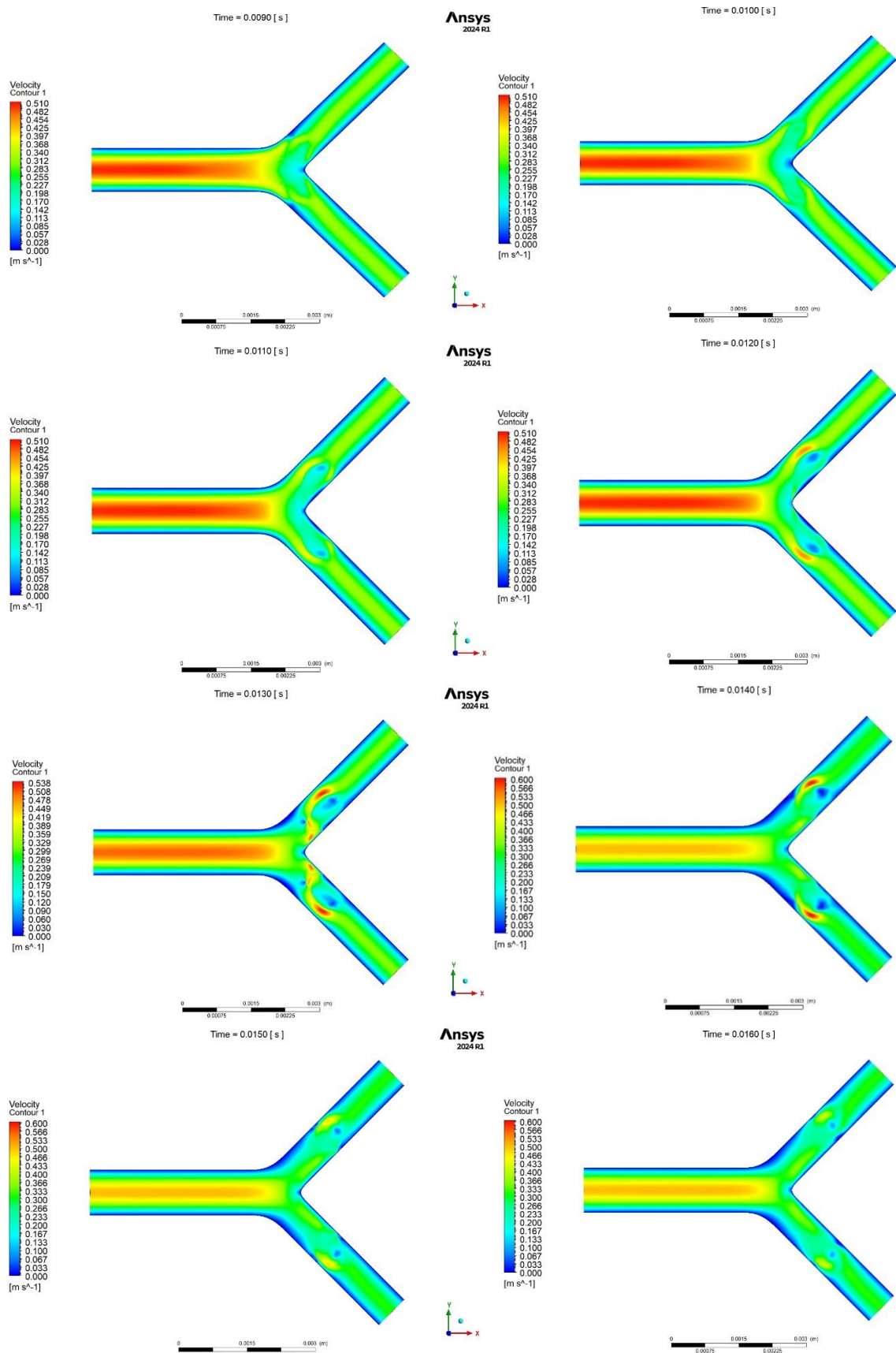
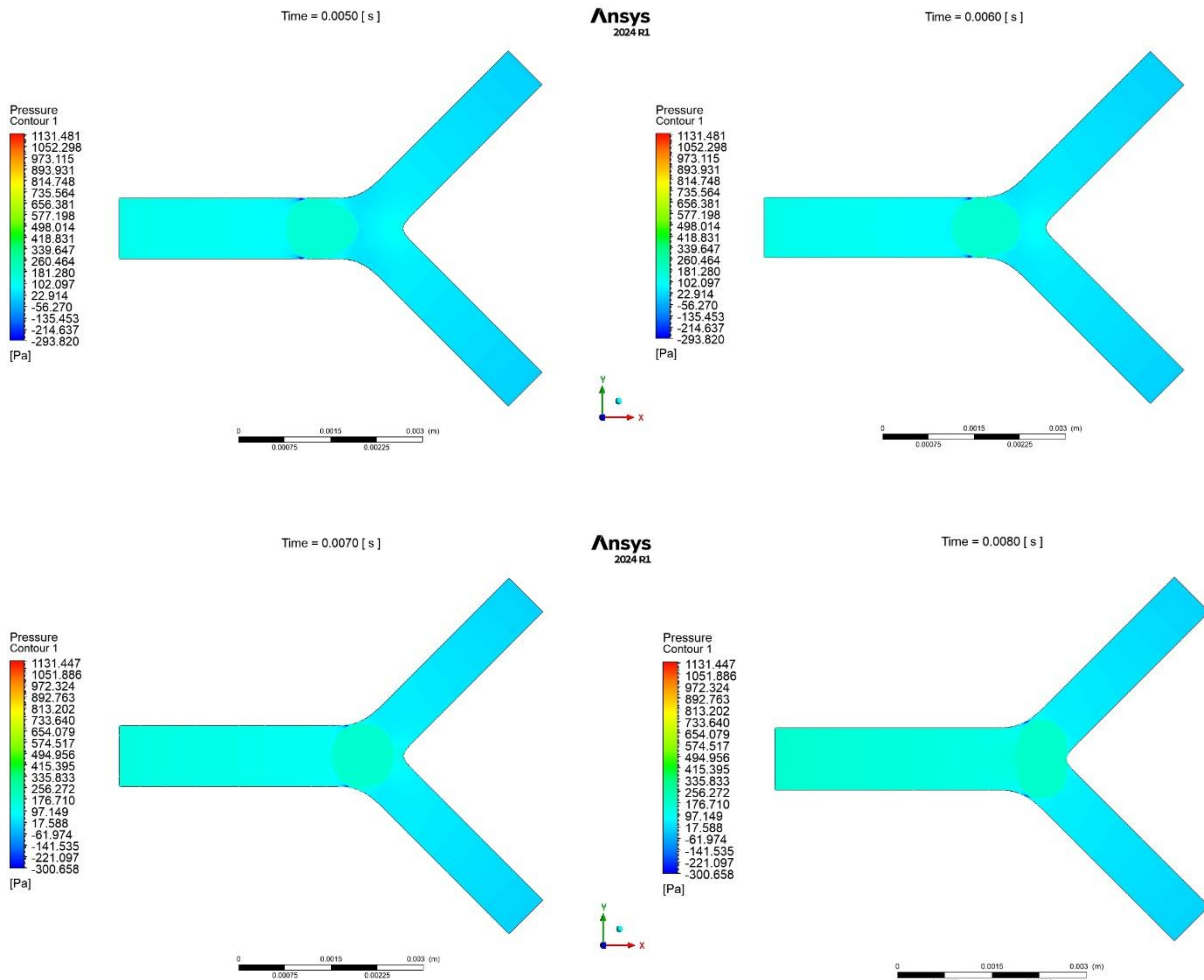


Figure 5-6: Velocity Contours at different time instances of 90° Bifurcation Vessel

Figure 5-6 illustrates how the flow behavior through a 90° bifurcation differs quite noticeably from the 60° case. Early on ( $t = 0.005\text{--}0.008$  s), the bubble enters the mother vessel with a noticeable boost in speed—about 18% higher centerline velocity, reaching up to 0.510 m/s. This increase is largely due to the sharper angle, which narrows the passage and forces the fluid to accelerate more quickly. As the bubble moves closer to the bifurcation point ( $t = 0.009\text{--}0.012$  s), three key features stand out. First, fast-moving jets form along the inner walls with sharper velocity gradients than in the 60° case. Second, the slower-moving zones near the outer walls known as stagnation regions are more widespread. Third, we see stronger vortex formation behind the bubble, with peak recirculation speeds around 0.255 m/s. These vortices don't last as long as those seen in the 60° geometry. When the bubble begins to split ( $t = 0.013\text{--}0.016$  s), the neck thins and ruptures more quickly completing the process in about 0.003 s, which is roughly faster than in the 60° case. Despite the faster dynamics, the division remains perfectly symmetrical.



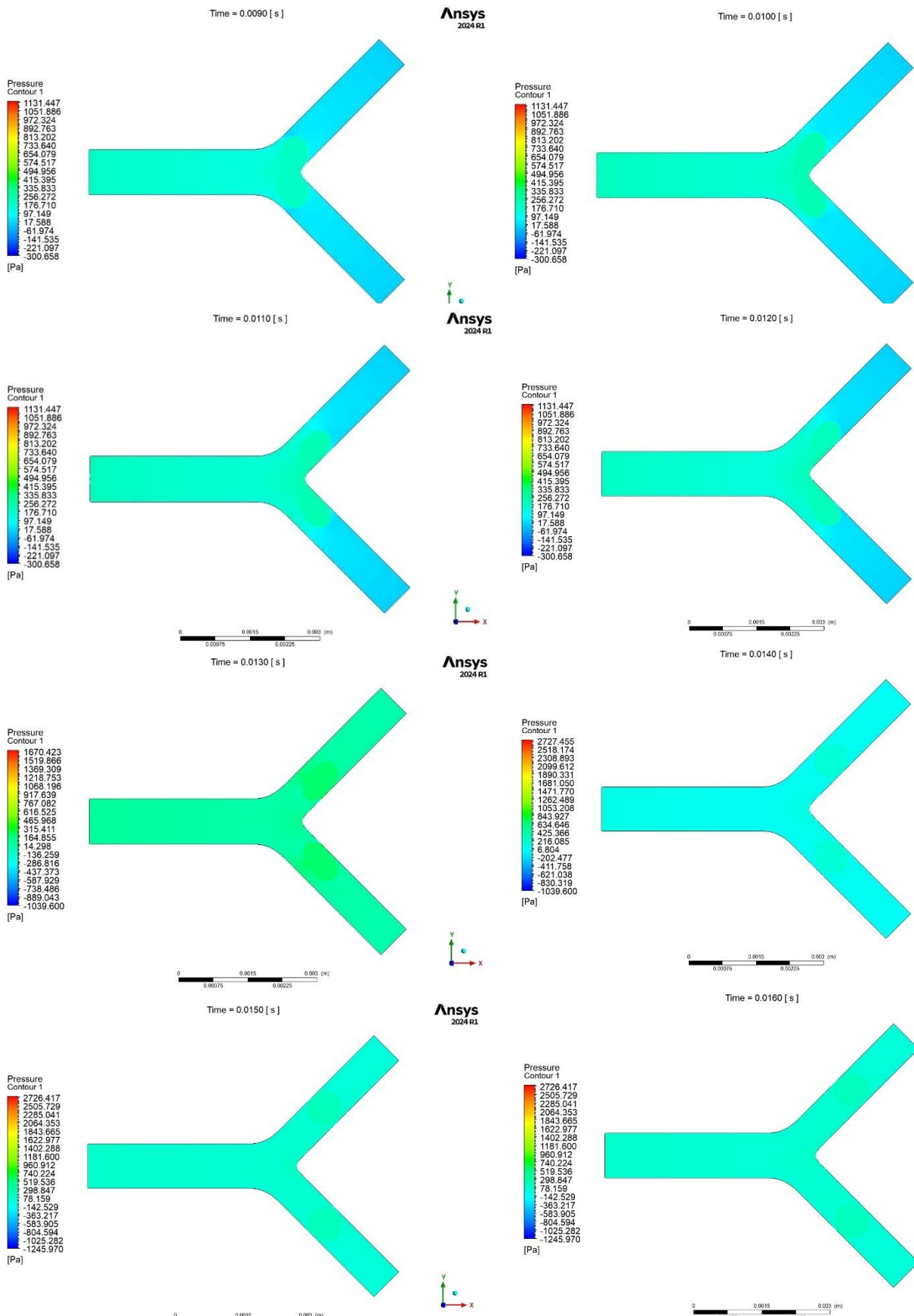


Figure 5-7: Pressure Contours at different time instances of 90° Bifurcation Vessel.

The pressure contours in Figure 5-7 show clear differences from the  $60^\circ$  case. Early in the bubble's transit ( $t = 0.005\text{--}0.008$  s), the pressure gradient reaches about 1425 Pa/mm, which is 28% steeper than in the  $60^\circ$  bifurcation. This stronger gradient helps drive faster initial flow, matching the earlier velocity findings. As the bubble nears the bifurcation ( $t = 0.009\text{--}0.012$  s), three main pressure zones appear: a high-pressure region along the inner walls, a transition zone at the center and a low-pressure region near the outer walls. The total pressure difference reaches 1425 Pa, higher than the 1187 Pa seen in the  $60^\circ$  case, contributing to sharper and more sudden flow redirection.

In the final phase ( $t = 0.013\text{--}0.016$  s), as the bubble begins to split, pressure levels change rapidly. The peak pressure jumps to 2727 Pa (vs. 2034 Pa in the  $60^\circ$  case), while negative pressure drops to  $-1246$  Pa. These shifts happen about 35% faster, indicating a more sudden and intense interaction with the vessel walls. The pressure follows a clear sequence: a sharp rise to 2727 Pa within 0.004 s, a short period where pressure stays high (above 2500 Pa), and then a quick drop to  $-1246$  Pa in just 0.0015 s. This final drop marks the point of bubble neck rupture and split. Overall, the  $90^\circ$  geometry leads to faster, stronger pressure changes, which may increase mechanical stress on the vessel walls compared to the  $60^\circ$  case.

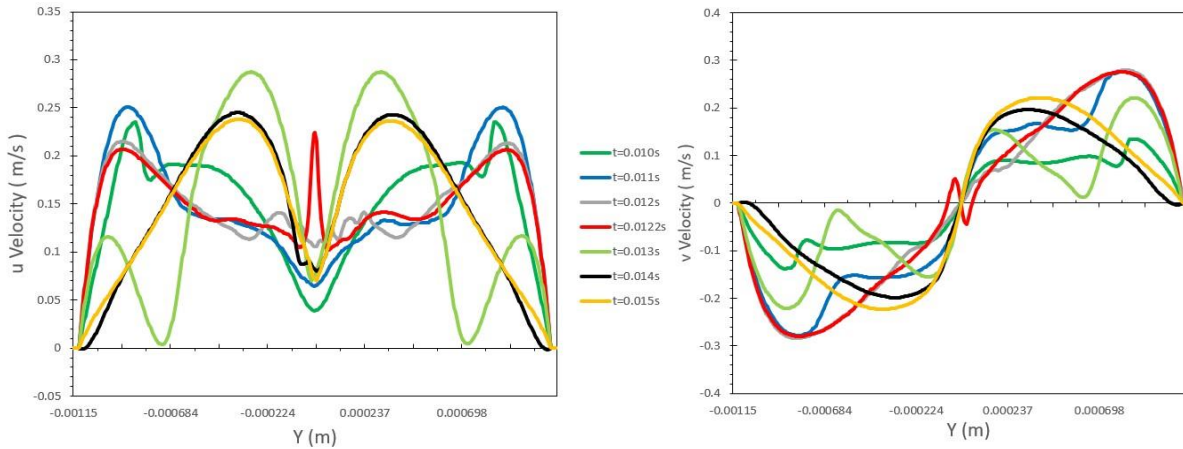


Figure 5-8: Velocity-u and Velocity-v Profiles of  $60^\circ$  Bifurcation Vessel.

Figure 5-4 highlights how velocity patterns in the  $90^\circ$  bifurcation differ markedly from the  $60^\circ$  case. As the bubble enters the bifurcation, axial velocity drops rapidly while transverse velocity remains low, indicating that the bubble initially blocks forward flow without immediate lateral diversion similar to the  $60^\circ$  case but more intense. At the bifurcation apex, forward flow stagnates 25% faster than in the  $60^\circ$  geometry. This is followed by the emergence of strong transverse flows, reaching up to 0.4 m/s, significantly higher than those in the gentler-angle

scenario. A key difference is the appearance of reverse flow zones near the outer walls—absent in the  $60^\circ$  case highlighting the sharper angle's more disruptive effect on flow direction. During the splitting phase, well-formed high-velocity jets appear along the inner walls, and large recirculation zones develop behind the bubble. These features are more symmetrical and intense than in the  $60^\circ$  configuration, leading to a quicker and more balanced division of the bubble. Post-splitting, the flow stabilizes faster, suggesting less downstream disturbance. Together with the pressure data, these velocity results confirm how the  $90^\circ$  bifurcation geometry produces sharper, more forceful, and more symmetric flow dynamics.

### 5.2.3 $120^\circ$ BIFURCATION ANGLE

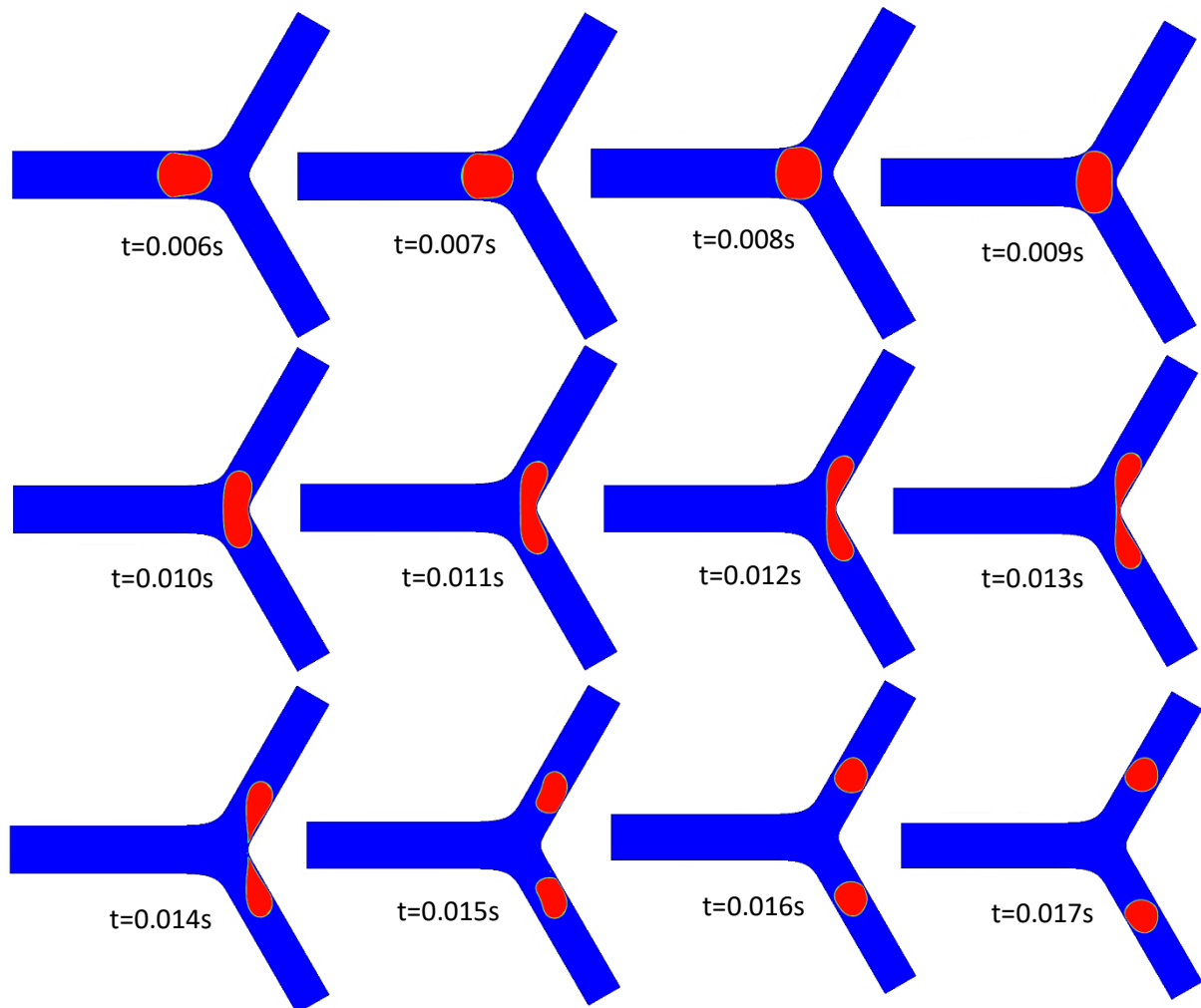
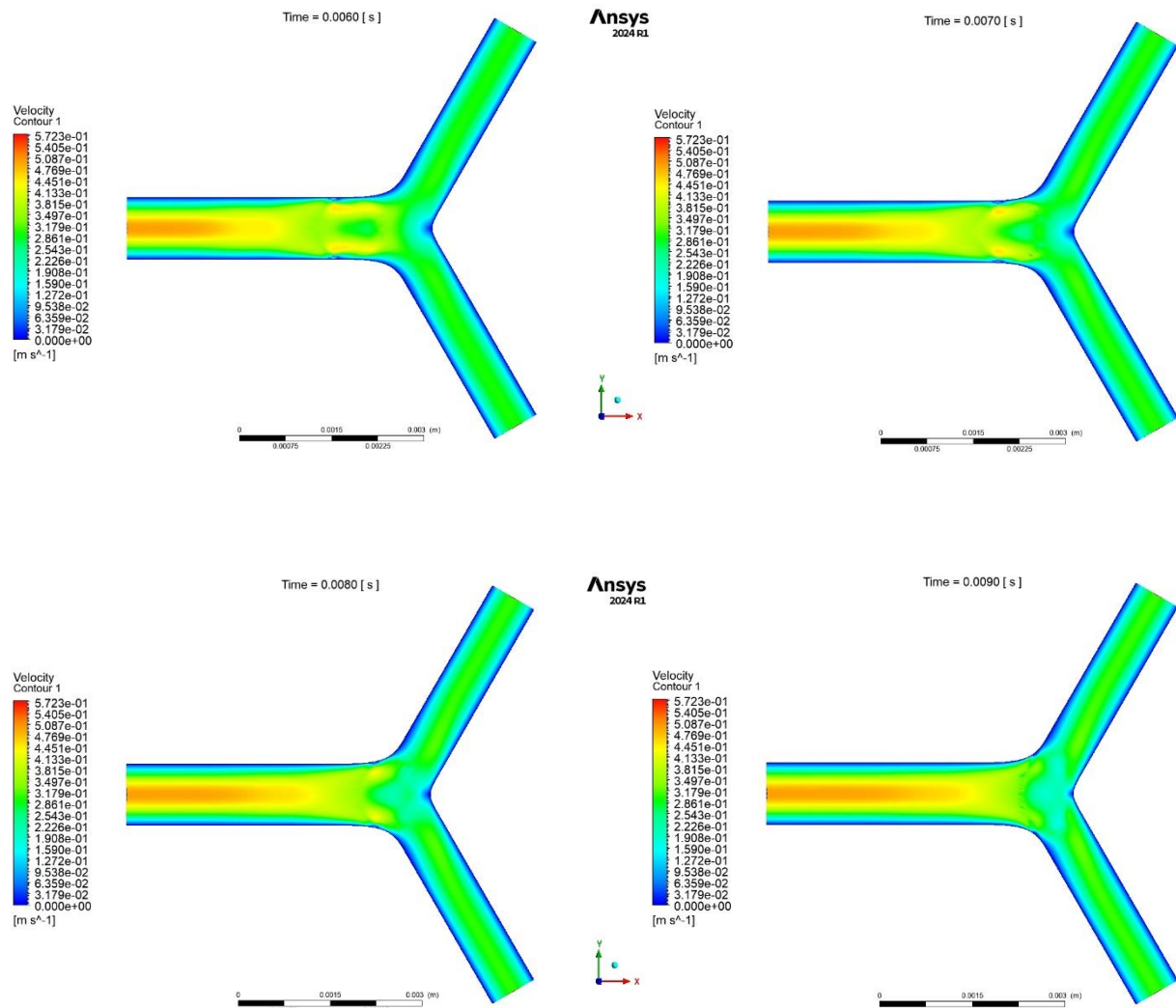


Figure 5-9: PFC bubble behavior at different time instances for  $90^\circ$  Bifurcation Vessel.

The  $120^\circ$  bifurcation shown in *Figure 5-9* creates a significantly different flow environment, resulting in distinct bubble dynamics compared to narrower bifurcation angles. The wider geometry alters both the shape and splitting behavior of the PFC gas bubble as it travels through the junction. In the initial phase of transit, the bubble retains its shape longer and exhibits noticeably less deformation at the trailing edge than in the  $90^\circ$  case. As it approaches the bifurcation, the front of the bubble begins to flatten. The trailing edge forms deeper concavities, more extreme than those seen in both  $60^\circ$  and  $90^\circ$  configurations. The splitting behavior in this wider geometry is also unique. Additionally, satellite bubbles consistently form during the splitting process, something rarely observed in sharper angles. Fragmentation of the bubble interface, particularly around the neck, is more frequent, and the overall timing of the breakup tends to vary, lacking the temporal consistency observed in  $60^\circ$  or  $90^\circ$  bifurcations.



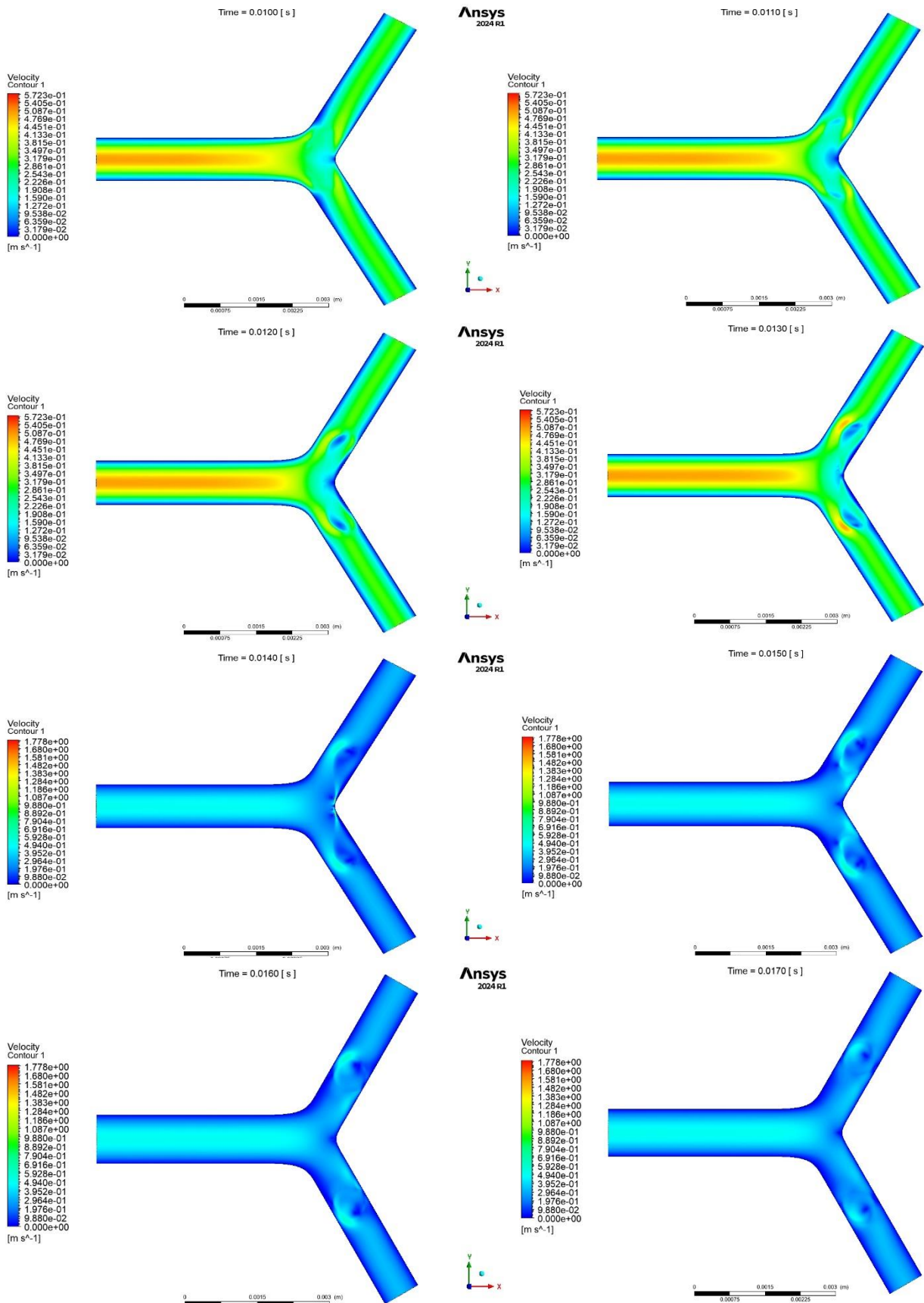
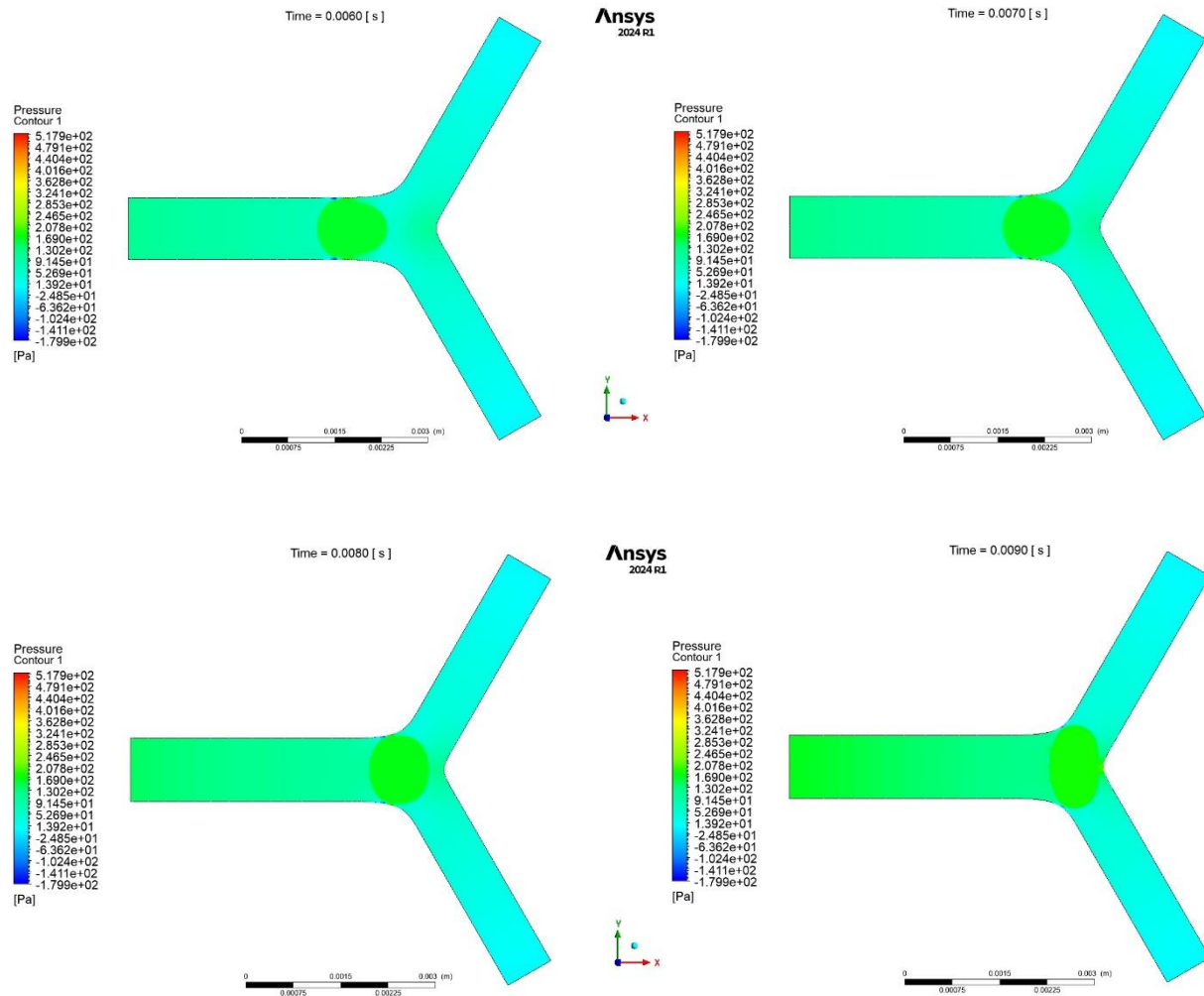


Figure 5-10: Velocity Contours of 120° Bifurcation Vessel at different time instances.

Figure 5-10 depicts that, the  $120^\circ$  angle creates more chaotic and unpredictable flow patterns compared to narrower bifurcations. As the bubble moves through the vessel, the fluid doesn't follow a smooth, organized path like it does in  $60^\circ$  or  $90^\circ$  cases. Instead, the flow becomes uneven, with some regions moving much faster than others. Near the inner walls, strong currents develop, but they spread out more widely rather than forming tight, high-speed jets. At the same time, large areas near the outer walls slow down significantly, creating "dead zones" where the fluid barely moves. Behind the bubble, swirling vortices form, but they are less stable than in narrower angles, often breaking apart or merging unpredictably. When the bubble reaches the splitting point, the flow becomes even more irregular. Unlike the  $60^\circ$  and  $90^\circ$  cases, where the division happens in a more controlled way, the  $120^\circ$  angle causes the bubble to stretch and thin unevenly. This leads to messy splitting, sometimes leaving behind small leftover bubbles.



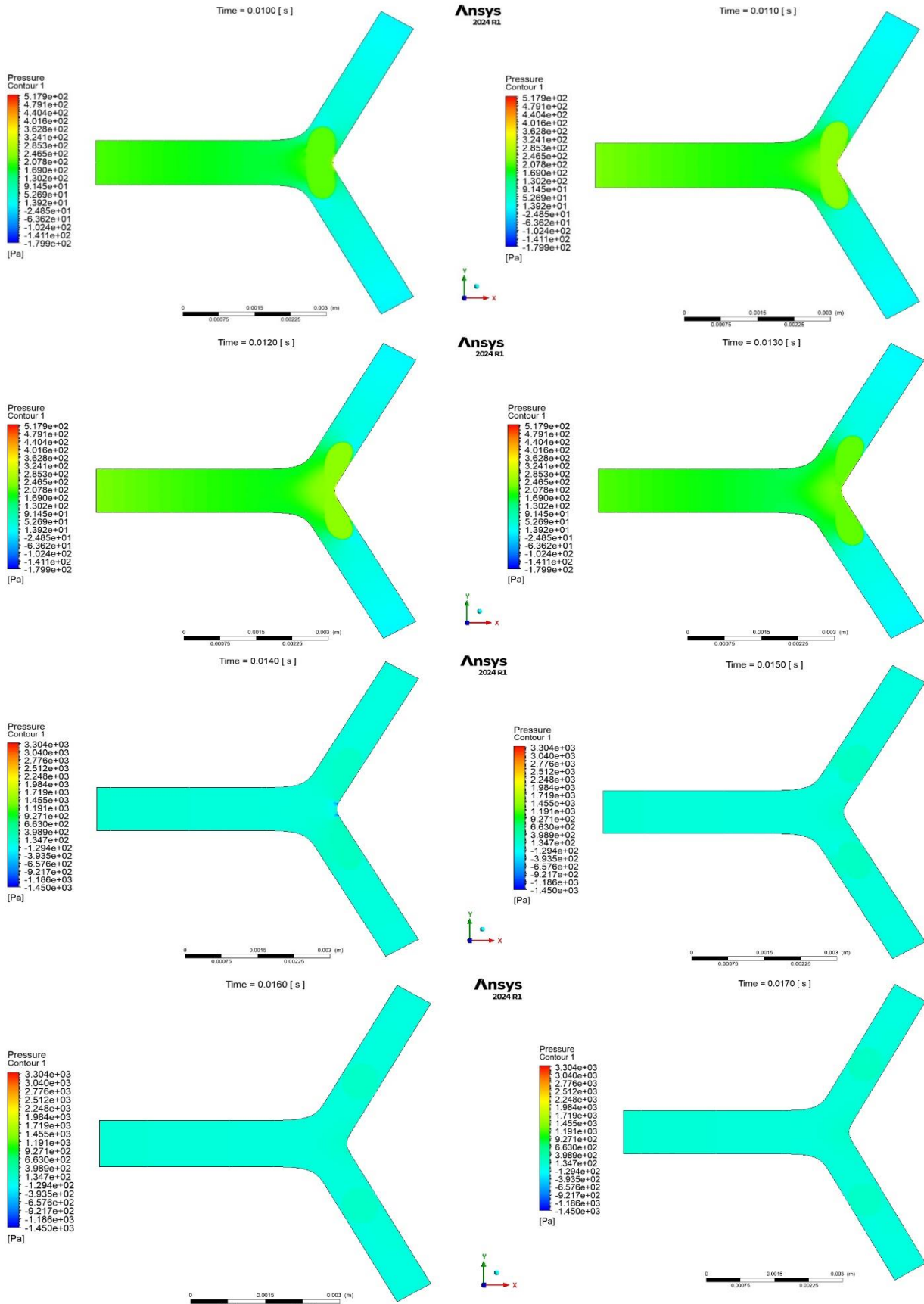


Figure 5-11: Pressure Contours at different time instances of 120° Bifurcation Vessel.

Figure 5-11 depicts the  $120^\circ$  bifurcation where the pressure behavior stands out distinctly from the sharper  $60^\circ$  and  $90^\circ$  cases. The wider angle leads to more gradual, widespread pressure changes throughout the vessel. Early on, the bubble experiences gentle and fairly balanced pressure from all directions, without any strong localized high or low zones. As it moves closer to the bifurcation, pressure begins to build unevenly along the bubble's surface, creating multiple peaks and pockets of lower pressure behind it. During the split, these changes become more diffused—there's no single, dramatic spike in pressure like in narrower angles. Instead, negative pressures develop slowly and span wider areas. In contrast, the  $60^\circ$  angle shows sharp, intense spikes in specific spots, and the  $90^\circ$  case features clear, rapid fluctuations. The  $120^\circ$  geometry, however, results in a more dispersed and milder pressure environment, highlighting how the vessel angle can significantly influence fluid dynamics.

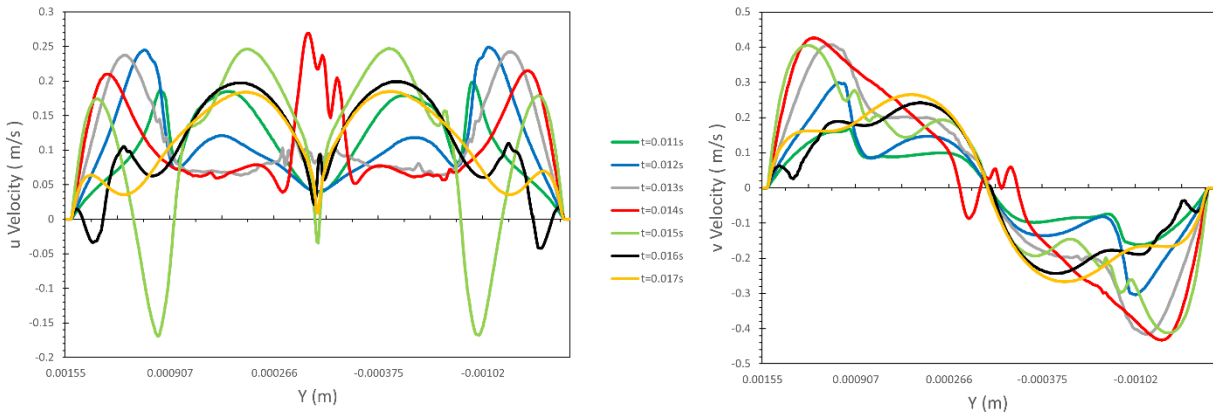


Figure 5-12: Velocity-u and Velocity-v Profiles of  $60^\circ$  Bifurcation Vessel.

The  $120^\circ$  angle creates chaotic, multidirectional flow patterns unlike narrower bifurcations. Fluid moves unpredictably, with frequent reversals and swirling motions spread across the vessel width. This turbulence causes erratic bubble movement and extended transit times. The unstable flow leads to inconsistent wall interactions, applying varying forces from multiple directions. Compared to  $60^\circ$  and  $90^\circ$  angles, the  $120^\circ$  geometry produces more disorganized flow development, significantly impacting bubble transport and vessel wall dynamics. These characteristics present unique challenges for medical applications requiring controlled fluid movement.

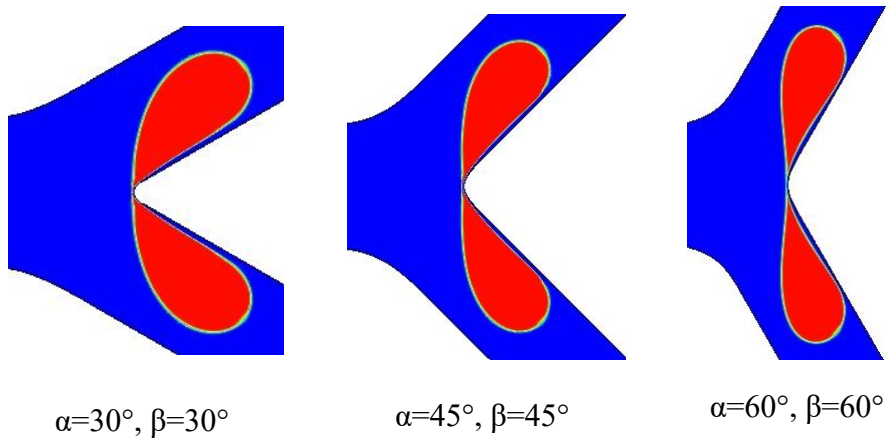


Figure 5-13: Splitting Behavior of vessels with varying angles.

Figure 5-12 shows for  $\alpha=30^\circ$ ,  $\beta=30^\circ$ , the bubble is convex shaped while splitting. For  $\alpha=45^\circ$ ,  $\beta=45^\circ$ , the shape is slightly concave and lastly for  $\alpha=60^\circ$ ,  $\beta=60^\circ$ , the concavity increases.

### 5.3 MODEL VALIDATION AGAINST PUBLISHED NUMERICAL STUDY

The numerical results obtained in the present study for  $Re = 100$  show agreement with the high Reynolds number cases ( $Re = 100$ ) reported by Nagargoje and Gupta (2020).

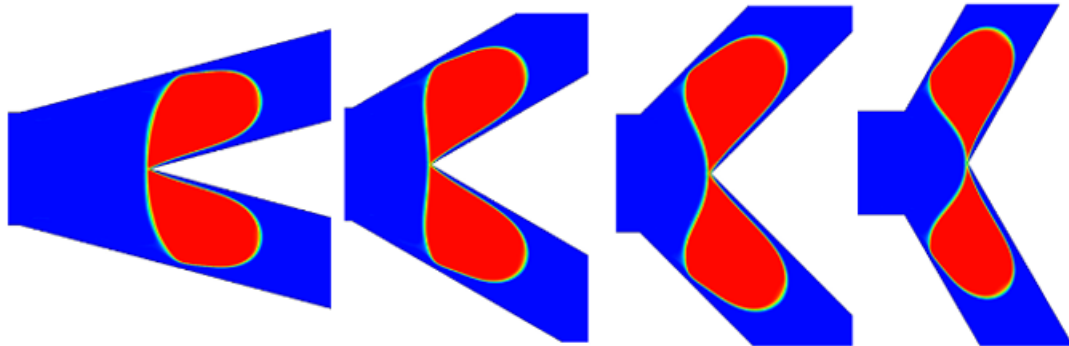
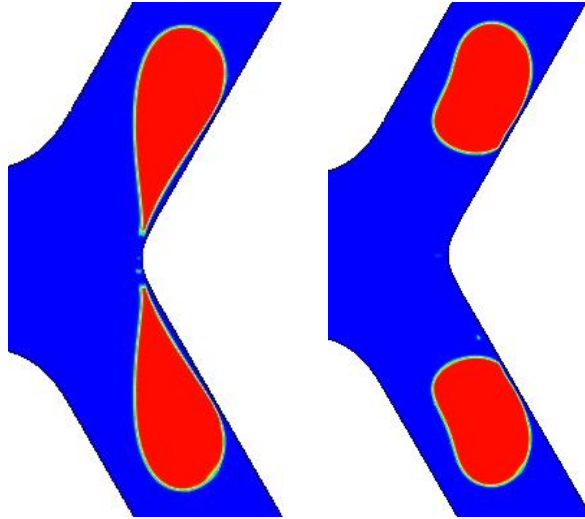


Figure 5-14 Splitting behavior of PFC bubble at the bifurcation point [39].

Figure 5-14 shows the Splitting behavior of PFC bubble at the bifurcation point, findings of Nagargoje and Gupta (2020), who investigated bubble transport and splitting dynamics in symmetric 2D bifurcations. It shows that the vessel with lower bifurcation angle has convexity near pinch off point. This convexity is turned into concavity with the gradual increment of bifurcation angles. As the bifurcation angle increases, the neck of the bubble becomes more concave. Almost similar behavior is found in my 3D simulation illustrated in Figure 5-13. They

also found that higher bifurcation angles increase the likelihood of retaining small satellite bubbles. This is mainly due to the formation of a thin, elongated tail that develops between the bubble's neck and the vessel wall during the splitting process. In wider angles like  $120^\circ$ , this tail often fails to fully detach, resulting in leftover fragments that remain near the bifurcation site [39]. In my simulation, I found traces of small satellites in  $120^\circ$  bifurcation vessel.



*Figure 5-15: Small satellites retaining in vessel of  $120^\circ$  bifurcation angle.*

Moreover, they showed homogeneous splitting of bubbles at  $Re = 100$  for all bifurcation angles which matches exactly with our simulations.

Therefore, key points of validation are:

### 1. Bubble Splitting Behavior:

- Both studies observed homogeneous splitting at  $Re=100$  for all bifurcation angles ( $30^\circ$ - $60^\circ$ )
- The bubble deformation patterns and pinch-off dynamics match closely
- No instances of non-splitting behavior were observed at  $Re= 00$  in either study.

### 2. Flow Characteristics:

- Pressure distributions show similar high-pressure zones at inner walls.
- Velocity profiles exhibit comparable symmetry during splitting.
- Final daughter bubble shapes match the reference results.

# CHAPTER 6

## CONCLUSIONS AND FUTURE WORK

### 6.1 CONCLUSIONS

This thesis investigated bubble transport and splitting dynamics in symmetric bifurcations with angles of 60°, 90°, and 120° at  $Re = 100$  using three-dimensional numerical simulations. The study successfully extended previous Newtonian findings to more physiologically realistic non-Newtonian conditions while maintaining agreement with fundamental splitting behaviors.

The key findings demonstrate:

#### **Bubble Splitting Behavior:**

- Satellite bubble formation was observed exclusively in 120° bifurcations.
- Homogeneous splitting occurred across all bifurcation angles (60°-120°), consistent with previous Newtonian studies.
- The transition from convex to concave neck shapes with increasing angle remained evident.

#### **Non-Newtonian Effects:**

- Shear-thinning behavior enhanced flow in narrow gaps between bubble and vessel walls.
- Modified local velocity gradients near bifurcation points.
- Produced slightly different bubble deformation rates compared to Newtonian cases.

#### **Angle-Dependent Phenomena:**

- 60° bifurcations produced the most stable and predictable splitting.
- 90° bifurcations showed faster splitting dynamics with symmetrical results.
- 120° bifurcations exhibited chaotic flow patterns and satellite formation.

#### **Validation with Non Newtonian Effects:**

- Shear-thinning behavior enhanced flow in narrow gaps between bubble and vessel walls
- Modified local velocity gradients near bifurcation points

- Produced slightly different bubble deformation rates compared to Newtonian cases.
- Verified the angle-dependent neck shape evolution and satellite formation.

Table 6-1: Comparative study of findings.

Parameter	60° Bifurcation	90° Bifurcation	120° Bifurcation	Validation Status	Non Newtonian Comparison
Splitting Type	Homogeneous	Homogeneous	Homogeneous	Confirmed	Consistent
Neck Shape	Convex	Transitional	Concave	Confirmed	Consistent
Satellite Formation	None	None	Present	Confirmed	Consistent
Splitting Time	Intermediate	Fastest	Slowest	N/A	Extended to 3D
Wall Interactions	Variable	Variable	Variable	Extended to 3D	Key Difference

While Nagargoje and Gupta (2020) used Newtonian blood assumptions, the current work demonstrates that their fundamental findings remain valid even when accounting for blood's non-Newtonian rheology, though with some quantitative modifications to local flow parameters.

## 6.2 FUTURE WORK

Future work recommendations might include:

- Investigation of bubble dynamics in patient-specific anatomical geometries reconstructed from medical imaging.
- Exploring pulsatile flow conditions to better mimic physiological blood flow patterns.
- Examine the effects of multiple sequential bifurcations on bubble transport.
- Systematically vary bubble-to-vessel diameter ratios.

# References

- [1] “Fluid mechanics,” *Wikipedia*. Sep. 09, 2024. Accessed: Jan. 15, 2025. [Online]. Available:  
[https://en.wikipedia.org/w/index.php?title=Fluid\\_mechanics&oldid=1244829667#cite\\_note-6](https://en.wikipedia.org/w/index.php?title=Fluid_mechanics&oldid=1244829667#cite_note-6)
- [2] “Fluid mechanics,” *Wikipedia*. Sep. 09, 2024. Accessed: Jan. 14, 2025. [Online]. Available:  
[https://en.wikipedia.org/w/index.php?title=Fluid\\_mechanics&oldid=1244829667](https://en.wikipedia.org/w/index.php?title=Fluid_mechanics&oldid=1244829667)
- [3] “Fluid Mechanics By Frank M. White - Solution - Chapter 3 □ Integral Relations for a Control Volume - Studocu.” Accessed: Jan. 14, 2025. [Online]. Available:  
<https://www.studocu.com/ph/document/university-of-the-visayas/bs-civil-engineering/fluid-mechanics-by-frank-m-white-solution/23493675>
- [4] G. K. Batchelor, *An Introduction to Fluid Dynamics*. in Cambridge Mathematical Library. Cambridge: Cambridge University Press, 2000. doi: 10.1017/CBO9780511800955.
- [5] “Fluid dynamics,” *Wikipedia*. Dec. 24, 2024. Accessed: Jan. 15, 2025. [Online]. Available:  
[https://en.wikipedia.org/w/index.php?title=Fluid\\_dynamics&oldid=1264877624#cite\\_note-J.D.\\_Anderson\\_2007-2](https://en.wikipedia.org/w/index.php?title=Fluid_dynamics&oldid=1264877624#cite_note-J.D._Anderson_2007-2)
- [6] N. Nangia, H. Johansen, N. A. Patankar, and A. P. S. Bhalla, “A moving control volume approach to computing hydrodynamic forces and torques on immersed bodies,” *J. Comput. Phys.*, vol. 347, pp. 437–462, Oct. 2017, doi: 10.1016/j.jcp.2017.06.047.
- [7] F. M. White, *Viscous fluid flow*, 3rd ed. New York, NY: McGraw-Hill Higher Education, 2006.
- [8] G. Bar-Meir, “Fundamentals of Compressible Fluid Mechanics”.
- [9] “Incompressible flow,” *Wikipedia*. Oct. 06, 2024. Accessed: Jan. 14, 2025. [Online]. Available:  
[https://en.wikipedia.org/w/index.php?title=Incompressible\\_flow&oldid=1249636699](https://en.wikipedia.org/w/index.php?title=Incompressible_flow&oldid=1249636699)
- [10] “The Motion of Bubbles and Drops in Reduced Gravity. By R. SHANKAR SUBRAMANIAN & R. BALASUBRAMANIAN. Cambridge University Press, 2001. 471 pp. ISBN 0 521 49605 5. £65.00.,” *J. Fluid Mech.*, vol. 453, pp. 439–443, Feb. 2002, doi: 10.1017/S0022112002257699.
- [11] *The Acoustic Bubble*. 1997. Accessed: Jan. 16, 2025. [Online]. Available:  
<https://shop.elsevier.com/books/the-acoustic-bubble/leighton/978-0-08-051876-3>
- [12] W. Lauterborn and T. Kurz, “Physics of bubble oscillations,” 2010, Accessed: Jan. 16, 2025. [Online]. Available: <https://publications.goettingen-research-online.de/handle/2/18876>
- [13] A. A. Kulkarni and J. B. Joshi, “Bubble Formation and Bubble Rise Velocity in Gas–Liquid Systems: A Review,” *Ind. Eng. Chem. Res.*, vol. 44, no. 16, pp. 5873–5931, Aug. 2005, doi: 10.1021/ie049131p.
- [14] H. Pang and G. Ngaile, “A Robust Bubble Growth Solution Scheme for Implementation in CFD Analysis of Multiphase Flows,” *Computation*, vol. 11, no. 4, p. 72, Mar. 2023, doi: 10.3390/computation11040072.

- [15] “Cavitation modelling,” *Wikipedia*. Aug. 24, 2024. Accessed: Jan. 16, 2025. [Online]. Available: [https://en.wikipedia.org/w/index.php?title=Cavitation\\_modelling&oldid=1241934011#cite\\_note-Plesset1977-2](https://en.wikipedia.org/w/index.php?title=Cavitation_modelling&oldid=1241934011#cite_note-Plesset1977-2)
- [16] “Cavitation modelling,” *Wikipedia*. Aug. 24, 2024. Accessed: Jan. 16, 2025. [Online]. Available: [https://en.wikipedia.org/w/index.php?title=Cavitation\\_modelling&oldid=1241934011](https://en.wikipedia.org/w/index.php?title=Cavitation_modelling&oldid=1241934011)
- [17] J. B. Keller and M. Miksis, “Bubble oscillations of large amplitude,” *J. Acoust. Soc. Am.*, vol. 68, no. 2, pp. 628–633, Aug. 1980, doi: 10.1121/1.384720.
- [18] J. L. Bull, “The application of microbubbles for targeted drug delivery,” *Expert Opin. Drug Deliv.*, vol. 4, no. 5, pp. 475–493, Sep. 2007, doi: 10.1517/17425247.4.5.475.
- [19] “Dynamics of Rising Bubbles and Their Impact with Viscoelastic Fluid Interfaces,” *Polymers*, vol. 14, no. 14, pp. 2948–2948, Jul. 2022, doi: 10.3390/polym14142948.
- [20] S.-P. Wang, A.-M. Zhang, Y.-L. Liu, S. Zhang, and P. Cui, “Bubble dynamics and its applications,” *J. Hydodyn.*, vol. 30, no. 6, pp. 975–991, Dec. 2018, doi: 10.1007/s42241-018-0141-3.
- [21] “Tortora, Derrickson: Principles of Anatomy and Physiology, 13th Edition - Student Companion Site.” Accessed: Jan. 17, 2025. [Online]. Available: <https://bcs.wiley.com/he-bcs/Books?action=chapter&bcsId=6205&itemId=0470565101&chapterId=66208>
- [22] “Hemodynamics,” *Wikipedia*. Nov. 29, 2024. Accessed: Jan. 17, 2025. [Online]. Available: [https://en.wikipedia.org/w/index.php?title=Hemodynamics&oldid=1260184514#cite\\_note-2](https://en.wikipedia.org/w/index.php?title=Hemodynamics&oldid=1260184514#cite_note-2)
- [23] “Physiology (Board Review Series) (3rd Edition) by Linda S. Costanzo | Open Library.” Accessed: Jan. 17, 2025. [Online]. Available: [https://openlibrary.org/books/OL8094719M/Physiology\\_%28Board\\_Review\\_Series%29\\_%283rd\\_Edition%29](https://openlibrary.org/books/OL8094719M/Physiology_%28Board_Review_Series%29_%283rd_Edition%29)
- [24] G. J. Tortora, *Principles of anatomy & physiology*. Hoboken, NJ : Wiley, 2012. Accessed: Jan. 17, 2025. [Online]. Available: [http://archive.org/details/principlesofanat0000tort\\_d4c9](http://archive.org/details/principlesofanat0000tort_d4c9)
- [25] B. Fagrell and J. Östergren, “Capillary Flow Measurements in Human Skin,” in *Clinical Investigation of the Microcirculation: Proceedings of the Meeting on Clinical Investigation of the Microcirculation held at London, England September, 1985*, J. E. Tooke and L. H. Smaje, Eds., Boston, MA: Springer US, 1987, pp. 23–33. doi: 10.1007/978-1-4613-2335-8\_2.
- [26] “Tortora, Derrickson: Principles of Anatomy and Physiology, 13th Edition - Student Companion Site.” Accessed: Jan. 17, 2025. [Online]. Available: <https://bcs.wiley.com/he-bcs/Books%20?action=index&bcsId=6205&itemId=0470565101>
- [27] E. N. Marieb and K. N. Hoehn, *Anatomy & Physiology*. Pearson Education, 2013.
- [28] “Munson, Young, Okiishi, Huebsch: Fundamentals of Fluid Mechanics, 6th Edition - Student Companion Site.” Accessed: Jan. 17, 2025. [Online]. Available: <https://bcs.wiley.com/he-bcs/Books?action=index&itemId=0470262842&bcsId=4532>

- [29] Y. C. Fung and B. W. Zweifach, “Microcirculation: Mechanics of Blood Flow in Capillaries,” *Annu. Rev. Fluid Mech.*, vol. 3, no. 1, pp. 189–210, Jan. 1971, doi: 10.1146/annurev.fl.03.010171.001201.
- [30] “Europe PMC.” Accessed: Jan. 17, 2025. [Online]. Available: <https://europepmc.org/article/MED/30855814>
- [31] “Biomechanics: Circulation | SpringerLink.” Accessed: Jan. 17, 2025. [Online]. Available: <https://link.springer.com/book/10.1007/978-1-4757-2696-1>
- [32] L. W. Markham, S. K. Knecht, S. R. Daniels, W. A. Mays, P. R. Khouri, and T. K. Knilans, “Development of exercise-induced arm-leg blood pressure gradient and abnormal arterial compliance in patients with repaired coarctation of the aorta,” *Am. J. Cardiol.*, vol. 94, no. 9, pp. 1200–1202, Nov. 2004, doi: 10.1016/j.amjcard.2004.07.097.
- [33] “Bubbles Moving in Blood Flow in a Microchannel Network: The Effect on the Local Hematocrit.,” *Micromachines*, vol. 11, no. 4, p. 344, Mar. 2020, doi: 10.3390/MI11040344.
- [34] “Acoustic bubble dynamics in a microvessel surrounded by elastic material,” *Phys. Fluids*, vol. 30, no. 1, p. 012104, Jan. 2018, doi: 10.1063/1.5005534.
- [35] K. Mukundakrishnan, P. S. Ayyaswamy, and D. M. Eckmann, “Finite-sized gas bubble motion in a blood vessel: Non-Newtonian effects,” *Phys. Rev. E*, vol. 78, no. 3, p. 036303, Sep. 2008, doi: 10.1103/PhysRevE.78.036303.
- [36] O. D. Kripfgans, C. M. Orifici, P. L. Carson, K. A. Ives, O. P. Eldevik, and J. B. Fowlkes, “Acoustic droplet vaporization for temporal and spatial control of tissue occlusion: a kidney study,” *IEEE Trans. Ultrason. Ferroelectr. Freq. Control*, vol. 52, no. 7, pp. 1101–1110, Jul. 2005, doi: 10.1109/TUFFC.2005.1503996.
- [37] W.-J. Yang, “Dynamics of gas bubbles in whole blood and plasma,” *J. Biomech.*, vol. 4, no. 2, pp. 119–125, Mar. 1971, doi: 10.1016/0021-9290(71)90022-4.
- [38] T. Ye and J. L. Bull, “Direct Numerical Simulations of Micro-Bubble Expansion in Gas Embolotherapy,” *J. Biomech. Eng.*, vol. 126, no. 6, pp. 745–759, Dec. 2004, doi: 10.1115/1.1824131.
- [39] M. S. Nagargoje and R. Gupta, *Numerical simulation of bubble transport and splitting dynamics for varying bifurcation angle*. SINTEF Academic Press, 2020. Accessed: Jan. 19, 2025. [Online]. Available: <https://sintef.brage.unit.no/sintef-xmlui/handle/11250/2720856>
- [40] A. Qamar, M. Warnez, D. T. Valassis, M. E. Guetzko, and J. L. Bull, “Small-bubble transport and splitting dynamics in a symmetric bifurcation,” *Comput. Methods Biomed. Engin.*, vol. 20, no. 11, pp. 1182–1194, Aug. 2017, doi: 10.1080/10255842.2017.1340466.
- [41] D. T. Valassis, R. E. Dodde, B. Esphuniyani, J. B. Fowlkes, and J. L. Bull, “Microbubble transport through a bifurcating vessel network with pulsatile flow,” *Biomed. Microdevices*, vol. 14, no. 1, pp. 131–143, Feb. 2012, doi: 10.1007/s10544-011-9591-x.
- [42] S. Samuel, A. Duprey, M. L. Fabiilli, J. L. Bull, and J. Brian Fowlkes, “*In Vivo* Microscopy of Targeted Vessel Occlusion Employing Acoustic Droplet Vaporization,” *Microcirculation*, vol. 19, no. 6, pp. 501–509, Aug. 2012, doi: 10.1111/j.1549-8719.2012.00176.x.

- [43] Z. Z. Wong, O. D. Kripfgans, A. Qamar, J. B. Fowlkes, and J. L. Bull, “Bubble evolution in acoustic droplet vaporization at physiological temperature via ultra-high speed imaging,” *Soft Matter*, vol. 7, no. 8, p. 4009, 2011, doi: 10.1039/c1sm00007a.
- [44] A. Qamar, Z. Z. Wong, J. B. Fowlkes, and J. L. Bull, “Dynamics of acoustic droplet vaporization in gas embolotherapy,” *Appl. Phys. Lett.*, vol. 96, no. 14, p. 143702, Apr. 2010, doi: 10.1063/1.3376763.
- [45] A. Carlson, M. Do-Quang, and G. Amberg, “Droplet dynamics in a bifurcating channel,” *Int. J. Multiph. Flow*, vol. 36, no. 5, pp. 397–405, May 2010, doi: 10.1016/j.ijmultiphaseflow.2010.01.002.
- [46] A. J. Calderon, B. Eshpuniyani, J. B. Fowlkes, and J. L. Bull, “A boundary element model of the transport of a semi-infinite bubble through a microvessel bifurcation,” *Phys. Fluids*, vol. 22, no. 6, p. 061902, Jun. 2010, doi: 10.1063/1.3442829.
- [47] A. Lo, O. Kripfgans, P. Carson, E. Rothman, and J. Fowlkes, “Acoustic droplet vaporization threshold: effects of pulse duration and contrast agent,” *IEEE Trans. Ultrason. Ferroelectr. Freq. Control*, vol. 54, no. 5, pp. 933–946, May 2007, doi: 10.1109/TUFFC.2007.339.
- [48] B. Eshpuniyani, J. B. Fowlkes, and J. L. Bull, “A bench top experimental model of bubble transport in multiple arteriole bifurcations,” *Int. J. Heat Fluid Flow*, vol. 26, no. 6, pp. 865–872, Dec. 2005, doi: 10.1016/j.ijheatfluidflow.2005.10.002.
- [49] J. Hanwright, J. Zhou, G. M. Evans, and K. P. Galvin, “Influence of Surfactant on Gas Bubble Stability,” *Langmuir*, vol. 21, no. 11, pp. 4912–4920, May 2005, doi: 10.1021/la0502894.
- [50] R. A. Hartunian and W. R. Sears, “On the instability of small gas bubbles moving uniformly in various liquids,” *J. Fluid Mech.*, vol. 3, no. 1, pp. 27–47, Oct. 1957, doi: 10.1017/S0022112057000464.
- [51] C. A. Ward, P. Tikuisis, and R. D. Venter, “Stability of bubbles in a closed volume of liquid-gas solution,” *J. Appl. Phys.*, vol. 53, no. 9, pp. 6076–6084, Sep. 1982, doi: 10.1063/1.331559.
- [52] G. K. Batchelor, “The stability of a large gas bubble rising through liquid,” *J. Fluid Mech.*, vol. 184, pp. 399–422, Nov. 1987, doi: 10.1017/S0022112087002945.
- [53] “Global stability analysis of bubbles rising in a vertical capillary with an external flow,” *J. Fluid Mech.*, vol. 958, Mar. 2023, doi: 10.1017/jfm.2023.123.
- [54] B. Podvin, S. Khoja, F. Moraga, and D. Attinger, “Model and experimental visualizations of the interaction of a bubble with an inclined wall,” *Chem. Eng. Sci.*, vol. 63, no. 7, pp. 1914–1928, Apr. 2008, doi: 10.1016/j.ces.2007.12.023.
- [55] J. Tihon, V. Pěnkavová, and J. Vejražka, “Wall shear stress induced by a large bubble rising in an inclined rectangular channel,” *Int. J. Multiph. Flow*, vol. 67, pp. 76–87, Dec. 2014, doi: 10.1016/j.ijmultiphaseflow.2014.07.005.
- [56] G. Losi and P. Poesio, “An experimental investigation on the effect of viscosity on bubbles moving in horizontal and slightly inclined pipes,” *Exp. Therm. Fluid Sci.*, vol. 75, pp. 77–88, Jul. 2016, doi: 10.1016/j.expthermflusci.2016.01.010.

- [57] H. Jeong and H. Park, “Near-wall rising behaviour of a deformable bubble at high Reynolds number,” *J. Fluid Mech.*, vol. 771, pp. 564–594, May 2015, doi: 10.1017/jfm.2015.191.
- [58] A. Zaruba, D. Lucas, H.-M. Prasser, and T. Höhne, “Bubble-wall interactions in a vertical gas–liquid flow: Bouncing, sliding and bubble deformations,” *Chem. Eng. Sci.*, vol. 62, no. 6, pp. 1591–1605, Mar. 2007, doi: 10.1016/j.ces.2006.11.044.
- [59] “Numerical simulation of bubble transport in a bifurcating microchannel: a preliminary study.,” *J. Biomech. Eng.-Trans. Asme*, vol. 134, no. 8, p. 081005, Aug. 2012, doi: 10.1115/1.4006975.
- [60] “Simulation analysis of blood flow in arteries of the human arm.” Accessed: Jan. 19, 2025. [Online]. Available: [https://www.researchgate.net/publication/319107439\\_Simulation\\_analysis\\_of\\_blood\\_flow\\_in\\_arteries\\_of\\_the\\_human\\_arm?\\_tp=eyJjb250ZXh0Ijp7ImZpcnN0UGFnZSI6Il9kaXJIY3QiLCJwYWdlIjoiX2RpcmVjdCJ9fQ](https://www.researchgate.net/publication/319107439_Simulation_analysis_of_blood_flow_in_arteries_of_the_human_arm?_tp=eyJjb250ZXh0Ijp7ImZpcnN0UGFnZSI6Il9kaXJIY3QiLCJwYWdlIjoiX2RpcmVjdCJ9fQ)

## **APPENDICES**

### **APPENDIX-A**

#### **Cost Estimation of the Project:**

Items	Cost (Taka)
Materials: i)	
ii)	
ii)	
iii)	

## APPENDIX-B

### Work/Activities Plan of the project/thesis using Gantt chart:

Work/ Activities	Week 1	Week 2	Week 3	Week 4	Week 5	Week 6	Week 7	Week 8	Week 9	Week 10	Week 11	Week 12	Week 13	Week 14-26
Study of the research paper														
Finding the research gap														
Fixing the objectives and research methodology														
Writing the project proposal														
Presenting a proposal														
Develop the design/process.														
Formulations and evaluations														
Results analysis														
Writing thesis														
Thesis correction and presentation preparation														
Final thesis presentation														

## APPENDIX-C

### Originality Report by Turnitin Plagiarism Software

[Document Viewer](#)

**Turnitin Originality Report**

Processed on: 29-Jun-2025 10:43 +06  
ID: 2707586978  
Word Count: 18168  
Submitted: 1  
1903082\_ME498.pdf By Chinmoy Deb Nath

<b>Similarity Index</b>	<b>19%</b>	<b>Similarity by Source</b>
		Internet Sources: 15% Publications: 9% Student Papers: 9%

mode:

2% match (student papers from 10-May-2023)  
[Submitted to Chittagong University of Engineering and Technology on 2023-05-10](#) x

2% match (Internet from 01-Jan-2025)  
["Hemodynamics", Wikipedia, en, 2025](#) x

1% match (student papers from 22-Jun-2023)  
Class: Project and Thesis  
Assignment: Journal Paper  
Paper ID: [2120825105](#) x

1% match (student papers from 10-May-2023)  
[Submitted to Chittagong University of Engineering and Technology on 2023-05-10](#) x

1% match (Internet from 01-Jan-2024)  
["Fluid dynamics", Wikipedia, en, 2024](#) x

1% match (Internet from 15-Dec-2021)  
[https://www.sintefbok.no/book/download/1271](#) x

<1% match (student papers from 22-Jun-2023)  
Class: Project and Thesis  
Assignment: Journal Paper  
Paper ID: [2120824597](#) x

<1% match (Internet from 07-Dec-2020)  
[https://en.wikipedia.org/wiki/Hemodynamics](#) x

<1% match (Internet from 18-Dec-2019)  
[https://en.wikipedia.org/wiki/Fluid\\_mechanics](#) x

<1% match (Internet from 30-Nov-2019)  
[https://en.wikipedia.org/wiki/Incompressible\\_fluid\\_flow](#) x

<1% match (Yang, Yi. "Electromechanical Characterization of Organic Field-Effect Transistors with Generalized Solid-State and Fractional Drift-Diffusion Models.", Purdue University, 2023)  
[Yang, Yi. "Electromechanical Characterization of Organic Field-Effect Transistors with Generalized Solid-State and Fractional Drift-Diffusion Models.", Purdue University, 2023](#) x

<1% match (Internet from 13-Jan-2023)  
[https://www.science.gov/topicpages/b/bubbly+flows+comparison.html](#) x

## APPENDIX-D

(This part will be filled/checked by the supervisor)

### CO-PO-K-P-A Mapping

PO1	Engineering knowledge: Apply the knowledge of mathematics, science, engineering fundamentals, and an engineering specialization to the solution of complex engineering problems.
PO2	Problem analysis: Identify, formulate, research literature, and analyze complex engineering problems reaching substantiated conclusions using first principles of mathematics, natural sciences, and engineering sciences.
PO3	Design/development of solutions: Design solutions for complex engineering problems and design system components or processes that meet the specified needs with appropriate consideration for public health and safety, and cultural, societal, and environmental considerations.
PO4	Conduct investigations of complex problems: Use research-based knowledge and research methods including design of experiments, analysis and interpretation of data, and synthesis of the information to provide valid conclusions.
PO5	Modern tool usage: Create, select, and apply appropriate techniques, resources, and modern engineering and IT tools including prediction and modeling to complex engineering activities with an understanding of the limitations.
PO6	The engineer and society: Apply reasoning informed by the contextual knowledge to assess societal, health, safety, legal, and cultural issues and the consequent responsibilities relevant to the professional engineering practice.
PO7	Environment and sustainability: Understand the impact of professional engineering solutions in societal and environmental contexts, and demonstrate the knowledge of, and need for sustainable development.
PO8	Ethics: Apply ethical principles and commit to professional ethics and responsibilities and norms of the engineering practice.
PO9	Individual and team work: Function effectively as an individual, and as a member or leader in diverse teams, and in multidisciplinary settings.
PO10	Communication: Communicate effectively on complex engineering activities with the engineering community and with society at large, such as being able to comprehend and write effective reports and design documentation, make effective presentations, and give and receive clear instructions.
PO11	Project management and finance: Demonstrate knowledge and understanding of the engineering and management principles and apply these to one's own work, as a member and leader in a team, to manage projects and in multidisciplinary environments.
PO12	Life-long learning: Recognize the need for, and have the preparation and ability to engage in independent and life-long learning in the broadest context of technological change.

Title of the Project: Computational Investigation of Perfluorocarbon-Gas Bubble Dynamics in Three-Dimensional Bifurcating Arteries.

Student ID: 1903082

		CO-PO-K-P-A Mapping																				Complex Engineering Problem Solving					Complex Engineering Activities						
		Program Outcomes									Knowledge Profile								Complex Engineering Problem Solving					Complex Engineering Activities									
		PO 1	P O 2	P O 3	P O 4	P O 5	P O 6	PO 7	P O 8	P O 9	P O 1 0	P O 1 1	P O 1 2	K1	K2	K3	K4	K5	K6	K7	K8	P1	P2	P3	P4	P5	P6	P7	A1	A2	A3	A4	A5
M E 49 8	Project and Thesis	Engineering Knowledge	Problem Analysis	Design/ Development of Solutions	Investigation	Modern Tool Usage	The Engineers & Society	Environment and Sustainability	Ethics	Individual and team work	Communication	Project Management and Finance	Life-long Learning	Science	Math	Engineering fundamentals	Engineering specialization	Design	Technology	Society	Research	Knowledge K3,K6,K8	Wide ranging/conflicting	No obvious solution	Infrequent issues	Outside problems	Diverse groups	Many components	Range of resources	Level of interaction	Innovation	Consequences	Familiarity
Needs complex engineering problem solution (p1+another P)																										Related to project							

